Monthly Notices
of the
ROYAL ASTRONOMICAL SOCIETY

MNRAS **486,** 21–41 (2019)
Advance Access publication 2019 March 16

doi:10.1093/mnras/stz774

Quasar Sightline and Galaxy Evolution (QSAGE) survey – I. The galaxy environment of O VI absorbers up to $z = 1.4$ around PKS 0232−04

R. M. Bielby,[1★] J. P. Stott,[2] F. Cullen,[3] T. M. Tripp,[4] J. N. Burchett,[5] M. Fumagalli,[1,6] S. L. Morris,[1] N. Tejos,[7] R. A. Crain,[8] R. G. Bower[6] and J. X. Prochaska[5]

[1]*Centre for Extra-galactic Astronomy (CEA), Durham University, South Road, Durham DH1 3LE, UK*
[2]*Department of Physics, Lancaster University, Lancaster LA1 4YB, UK*
[3]*Institute for Astronomy, University of Edinburgh, Royal Observatory, Edinburgh EH9 3HJ, UK*
[4]*Department of Astronomy, University of Massachusetts – Amherst, Amherst, MA 01003, USA*
[5]*UCO/Lick Observatory, University of California, Santa Cruz, CA 95064, USA*
[6]*Institute for Computational Cosmology (ICC), Durham University, South Road, Durham DH1 3LE, UK*
[7]*Instituto de Física, Pontificia Universidad Católica de Valparaíso, Casilla 4059, Valparaíso, Chile*
[8]*Astrophysics Research Institute, Liverpool John Moores University, 146 Brownlow Hill, Liverpool L3 5RF, UK*

Accepted 2019 March 7. Received 2019 February 15; in original form 2018 September 14

ABSTRACT

We present the first results from a study of O VI absorption around galaxies at $z < 1.44$ using data from a near-infrared grism spectroscopic *Hubble Space Telescope* Large Programme, the Quasar Sightline and Galaxy Evolution (QSAGE) survey. QSAGE is the first grism galaxy survey to focus on the circumgalactic medium at $z \sim 1$, providing a blind survey of the galaxy population. The galaxy sample is Hα flux limited ($f(\mathrm{H}\alpha) > 2 \times 10^{-17}$ erg s^{-1} cm^{-2}) at $0.68 < z < 1.44$, corresponding to $\gtrsim$0.2–0.8 M$_\odot$ yr^{-1}. In this first of 12 fields, we combine the galaxy data with high-resolution STIS and COS spectroscopy of the background quasar to study O VI in the circumgalactic medium. At $z \sim 1$, we find O VI absorption systems up to $b \sim 350$ kpc ($\sim 4R_{\rm vir}$) from the nearest detected galaxy. Further, we find ∼50 per cent of $\gtrsim$1 M$_\odot$ yr^{-1} star-forming galaxies within $2R_{\rm vir}$ show no associated O VI absorption to a limit of at least $N(\mathrm{O\,VI}) = 10^{13.9}$ cm^{-2}. That we detect O VI at such large distances from galaxies and that a significant fraction of star-forming galaxies show no detectable O VI absorption disfavours outflows from ongoing star formation as the primary medium traced by these absorbers. Instead, by combining our own low- and high-redshift data with existing samples, we find tentative evidence for many strong ($N(\mathrm{O\,VI}) > 10^{14}$ cm^{-2}) O VI absorption systems to be associated with $M_\star \sim 10^{9.5\text{–}10}$ M$_\odot$ mass galaxies ($M_{\rm halo} \sim 10^{11.5\text{–}12}$ M$_\odot$ dark matter haloes), and infer that they may be tracing predominantly collisionally ionized gas within the haloes of such galaxies.

Key words: galaxies: distances and redshifts – intergalactic medium – quasars: absorption lines.

1 INTRODUCTION

The peak epoch in the volume-averaged star formation rate (SFR) for galaxies is at $z = 1$–2 with the SFR in typical galaxies being an order of magnitude higher than in the local Universe (e.g. Lilly et al. 1996; Madau et al. 1996; Sobral et al. 2013). A picture is emerging in which star formation at this epoch is very different to that at the present day. Rather than the subdued formation of stars that is the norm in today's Universe, violent episodes of star formation are driven by the formation of superstar clusters within unstable gas-rich discs (e.g. Swinbank et al. 2010; Tacconi et al. 2010).

Theory suggests that the peak in the star formation rate density is the result of a higher rate of gas accretion in the early Universe (e.g. Dekel et al. 2009; Lagos et al. 2011; van de Voort et al. 2011). Star formation at high redshift should be critically dependent on the inflow rate of cold gas, whilst the present-day galaxy stellar mass function is most readily explained through an efficient feedback mechanism such as strong supernovae driven outflows. In order to fully understand the interplay and balance of these factors (e.g.

★ E-mail: richard.bielby@durham.ac.uk

Bouché et al. 2010; Davé, Finlator & Oppenheimer 2012), it is crucial that we test these theories by detecting diffuse baryons inside and around the haloes of galaxies, charting their abundance and physical properties as a function of redshift (e.g. Fumagalli et al. 2011; Davé et al. 2012; Hummels et al. 2013; Rahmati et al. 2013, 2015; Correa et al. 2018; Oppenheimer et al. 2018b). The approximate area of influence, within which a galaxy deposits and receives baryonic material, is commonly referred to as the circumgalactic medium (CGM).

Extensive studies have been performed using the powerful combination of galaxy surveys with high-resolution quasar sightline data, to analyse the nature of gas around galaxies at $z \lesssim 1$ (e.g. Bergeron & Boissé 1991; Morris et al. 1991; Morris et al. 1993; Steidel, Dickinson & Persson 1994; Chen et al. 1998, 2001; Steidel et al. 2002; Chen & Mulchaey 2009; Crighton et al. 2010; Prochaska et al. 2011; Tumlinson et al. 2011; Bouché et al. 2012; Kacprzak, Churchill & Nielsen 2012; Nielsen, Churchill & Kacprzak 2013; Tejos et al. 2014; Finn et al. 2016; Prochaska et al. 2017) and at $2 \lesssim z \lesssim 4$ (primarily using the Lyman Break method; e.g. Adelberger et al. 2003, 2005; Simcoe et al. 2006; Chen et al. 2010; Crighton et al. 2011; Rakic et al. 2012; Prochaska et al. 2013; Prochaska, Lau & Hennawi 2014; Tummuangpak et al. 2014; Turner et al. 2015; Fumagalli et al. 2016, 2017b; Turner et al. 2017; Bielby et al. 2017b). These have provided important insights for understanding the flow of baryons around galaxies and how this impacts galaxy evolution. However, the available data *between* these two epochs (i.e. $z \approx 1$–2) is more limited, and primarily focused around either Ly α absorption or relatively low-ion absorbers such as Mg II and C IV (e.g. Chen et al. 1998; Bowen et al. 2006; Morris & Jannuzi 2006; Rubin et al. 2010; Lovegrove & Simcoe 2011; Farina et al. 2014; Johnson, Chen & Mulchaey 2015b). There are an increasing number of studies focusing on the relevance of large-scale structure (i.e. voids, filaments, groups, and clusters) with respect to observations of the CGM (e.g. Penton, Stocke & Shull 2002; Aracil et al. 2006; Tejos et al. 2012, 2016; Stocke et al. 2014; Burchett et al. 2016, 2018; Fumagalli et al. 2016, 2017b; Bielby et al. 2017a; Péroux et al. 2017; Fynbo et al. 2018; Pessa et al. 2018). Such studies are adding important context to for interpreting CGM observations, but are again primarily limited to $z \lesssim 0.5$ or $z > 2$.

The O VI doublet absorption feature offers important insights into galaxy evolution (Tripp, Savage & Jenkins 2000). Low-redshift studies have shown that O VI absorbers often trace 0.1–1 L$*$ star-forming galaxy haloes (Chen & Mulchaey 2009; Wakker & Savage 2009). The nature of the material traced by O VI absorption in quasar sightlines potentially traces a broad range of physical manifestations: as outflowing material, indicative of ongoing or recent star formation (e.g. Tumlinson et al. 2011; Meiring et al. 2013; Werk et al. 2016); diffuse halo gas at the ambient halo temperature (e.g. Oppenheimer et al. 2016; Werk et al. 2016; Nielsen et al. 2017; Oppenheimer et al. 2018a; Kacprzak et al. 2019); intragroup material (e.g. Stocke et al. 2014, 2017; Pointon et al. 2017); or more widely spread warm-hot intergalactic medium (e.g. Shull, Smith & Danforth 2012).

In this paper, we present results from the first field analysed as part of the Quasar Sightline and Galaxy Evolution (QSAGE) survey. We have performed a grism spectroscopic survey around 12 bright quasars at $z > 1.2$, all with existing archival *HST*/STIS, and in some cases *HST*/COS, spectroscopy. By selecting quasar sightlines as target fields, we place the scientific focus on studying the CGM, whilst providing 12 effectively independent pencil beam surveys suitable for a wide range of galaxy evolution science. Whilst the *HST*/STIS and *HST*/COS data probe gas in absorption along the central sightline at $z \lesssim 1.44$, our new *HST* WFC3 grism observations survey the galaxy population 'blindly' (i.e. without any preselection aside from flux limits) around these sightlines across a comparable redshift range (predominantly via H α emission). In an earlier paper (Bielby et al. 2017a), we presented an analysis of Mg II absorption associated with a group environment detected in MUSE observations on one of the fields, prior to having acquired WFC3/grism data. Here we focus on a second field, this time incorporating both MUSE IFU and WFC3 grism data, whilst also presenting the survey strategy, data-processing methods, and an analysis of the relationship between O VI absorption and galaxies at $0.68 < z < 1.4$ data. The quasar that forms the basis for this study is PKS 0232−04 (Shimmins et al. 1966, originally designated PHL 1377; Haro & Luyten 1962) at a redshift of $z = 1.44$.

In Section 2 we present the observations and data reduction methods (including optical and NIR imaging, grism spectroscopy, IFU spectroscopy with MUSE, and high-resolution sightline spectroscopy); in Section 3, we present an analysis of the distribution of galaxies around O VI absorbers as a function of galaxy properties and environment; we discuss our results in Section 4; and in Section 5 we give our conclusions and a summary. Throughout this paper, we use the AB magnitude system and the Planck 2015 cosmology (Planck Collaboration XIII 2016). Unless otherwise stated, all distances are given in proper coordinates.

2 OBSERVATIONS

The QSAGE survey targets 12 $z \gtrsim 1.2$ quasars with the aim of mapping and characterizing the galaxy populations in their foregrounds (*HST* Large Programme 14594; PIs: R. Bielby, J. P. Stott). The full survey consists of 96 orbits with the WFC3 in imaging and grism mode (i.e. 8 h per quasar sightline). In this paper we focus on the first field to be fully analysed, centred on the $z = 1.44$ quasar PKS 0232−04, chosen due to the extensive data available to complement the WFC3 grism and STIS sightline data: Canada–France–Hawaii Telescope Legacy Survey (CFHTLS) optical imaging, MUSE IFU data and *HST*/COS sightline spectroscopy. In the following section we describe in detail the methods used in taking and processing the various observations on this first target field, and which going forward will be used across the entirety of the 12 survey fields.

We note that this sightline was previously observed with *HST* + FOS (Jannuzi et al. 1998), which showed that the sightline is free of LLS and therefore maximizes the path-length for FUV ions such as Ne VIII and Mg X. However, this pre-selection also means that the survey imposes a strong bias against some critical components of the CGM at $z > 0.4$ (see discussion in Tumlinson et al. 2013 for example), namely LLS and stronger H I systems. Many LLS exhibit coincident O VI absorption and so this is relevant even for a focus on high-ionization state gas (though a small fraction of O VI absorbers globally, LLS are common at $\lesssim$150 kpc from $>$0.1 L$*$ galaxies of all types).

2.1 *HST* WFC3 data

For a single field, the QSAGE *HST* observations consist of eight grism exposures alongside supporting NIR imaging. The imaging is required for the identification of accurate source coordinates, which act as the basis for the extraction of object spectra from the grism data. The observations for a given field were split into four 'visits', with each visit providing observations at a different position angle. Each visit consisted of two orbits, with each orbit

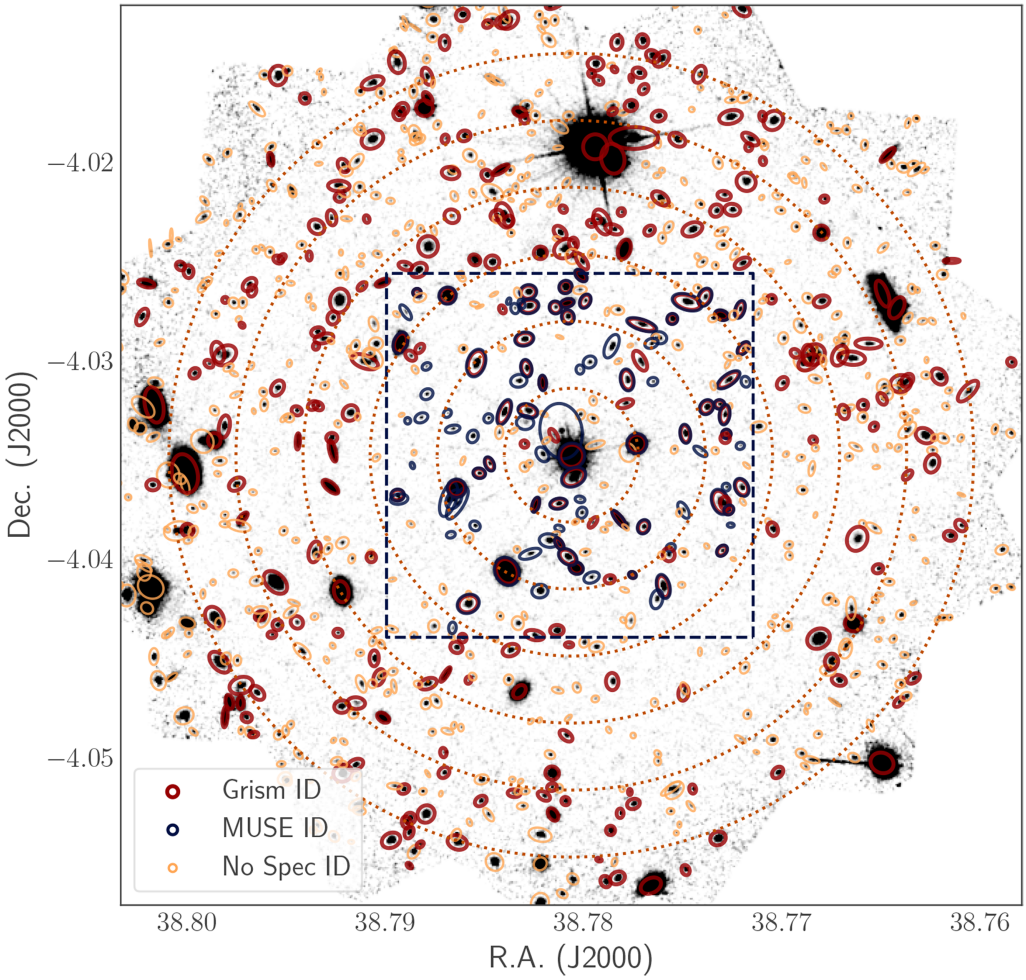

Figure 1. Stacked *HST*/WFC3 broad-band *F*140*W* image from the four separate orbits observing PKS 0232−04. Galaxies with a successfully identified redshift from either VLT/MUSE (blue ellipses) or *HST*/WFC3 grism observations (dark red ellipses) are marked. Objects detected in the imaging, but without a reliably identified redshift are marked by the pale orange ellipses. Dotted rings indicate scales of 100 kpc up to 600 kpc in steps of 100 kpc at $z = 1$. The dashed box denotes the field of view of the VLT/MUSE observations.

scheduled to acquire a single *F*140*W* image of ≈250 s, two exposures of ≈1000 s using the G141 grism, and a single ≈250 s *F*160*W* exposure. These exposures were taken using the 'SPARS25' sampling sequence in the case of the basic imaging exposures and the 'SPARS100' sampling sequence in the case of the grism exposures. The corresponding exposure times were tweaked to optimally fill the time afforded by a given orbit and all exposures were taken with the 'grism1024' aperture. The total exposure times across the four visits for this field were 2123 s with *F*140*W*; 2123 s with *F*160*W*; and 16 047 s with the G141 grism. These data represent some of the deepest observations using the WFC3 G141 grism thus far. As such, the different position-angle visits are necessary for the optimal extraction of spectra with the removal of contamination from overlapping sources.

2.1.1 WFC3 NIR imaging

Both the direct imaging and grism data were reduced using GRIZLI (Brammer, in prepararion[1]), a custom software package dedicated to the reduction and analysis of slitless spectroscopic datasets which builds on previous software packages such as AXE (Kümmel et al. 2009) and THREEDHST (Brammer et al. 2012; Momcheva et al. 2016). For the direct images, individual exposures were corrected for small astronomic offsets using TWEAKREG before ASTRODRIZZLE was used to produce background-subtracted drizzled images in both the *F*140*W* and *F*160*W* filters. The *F*140*W* and *F*160*W* sets of images were each stacked using SWARP (Bertin et al. 2002) using a median combination. The resulting *F*140*W* stacked image is shown in Fig. 1. Photometric zero-points for the *F*140*W* and *F*160*W* imaging were taken directly from the STScI guidelines [$m_{ZP}(F140W) = 26.45$ and $m_{ZP}(F160W) = 25.95$].

Extraction of the grism spectra requires a catalogue of sources with accurate positions from the associated imaging data. We produced this catalogue from the *F*140*W* stacked image using SExtractor (Bertin & Arnouts 1996). We used a detection threshold of 1.5σ, a minimum area for detection of five contiguous pixels, and we adjusted the deblending parameter to optimally extract any objects visually identified as being blended with the quasar point spread function (DEBLEND_MINCONT = 0.005).

The number counts of sources detected in the WFC3 *F*140*W* and *F*160*W* imaging are given in the final two panels of Fig. 2,

[1] https://github.com/gbrammer/grizli

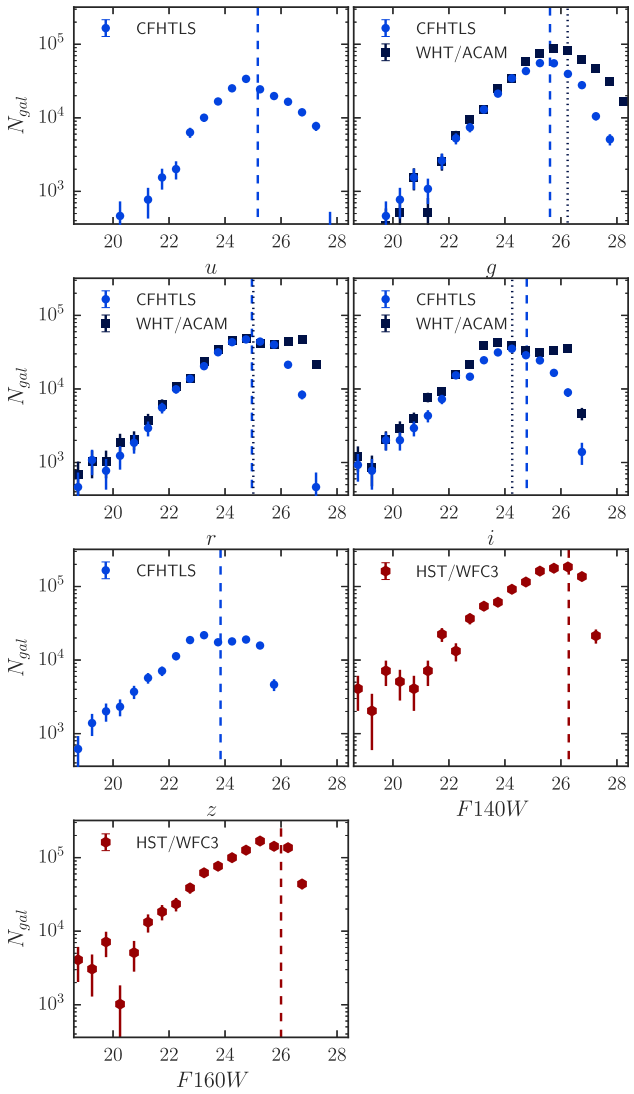

Figure 2. Galaxy number counts estimated for all of the broad-band imaging used in this work, obtained from single image source extraction using SExtractor. Vertical lines show the estimated 80 per cent completeness limit for point sources. Where both CFHTLS and WHT/ACAM data are available, the dashed line denotes the CFHTLS limit and the dotted line shows the WHT/ACAM limit.

whilst the corresponding 80 per cent completeness depths are given in Table 1. The completeness estimates were made by iteratively placing model sources (Gaussian profiles with the instrument full width at half-maximum – FWHM) directly into the imaging data, and re-running SExtractor with our given parameters on these modified images.

2.2 WFC3 G141 grism data

The catalogues and segmentation images generated with SExtractor were then used to extract the spectrum of each object using grizli. First, each G141 exposure was divided through by the *F*140*W* flat-field, neglecting any wavelength-dependent flat-field effects which are at most a few per cent (Momcheva et al. 2016). An initial background was subtracted using the 'master sky' images from Brammer, Ryan & Pirzkal (2015). These master images are necessary to account for the variation in background structure

Table 1. Overview of the imaging data used in this paper. Completeness estimates are based on an 80 per cent limit for point sources (with a 2σ detection threshold). Values for the CFHTLS data are reproduced directly from the CFHTLS synoptic table.

Instrument	Filter	IQ (arcsec)	Completeness (80 per cent, Mag)
WHT/ACAM	$g_{\rm sdss}$	0.87	26.24
WHT/ACAM	$r_{\rm sdss}$	0.88	25.01
WHT/ACAM	$i_{\rm sdss}$	0.88	24.26
CFHT/MegaCAM	$u_{\rm cfht}$	0.90	25.17
CFHT/MegaCAM	$g_{\rm cfht}$	0.74	25.61
CFHT/MegaCAM	$r_{\rm cfht}$	0.72	24.96
CFHT/MegaCAM	$i_{\rm cfht}$	0.68	24.78
CFHT/MegaCAM	$z_{\rm cfht}$	0.72	23.84
HST/WFC3	*F*140*W*	0.26	26.28
HST/WFC3	*F*160*W*	0.29	26.00

due to variations in zodiacal continuum, scattered light, and He emission across the sky (Momcheva et al. 2016). The remaining residuals (typically 0.5–1 per cent of the initial background levels) were then removed by subtracting average values of the sky pixels in each column. Finally 1D and 2D spectra were extracted from the background-subtracted grism images at the individual exposure level, which, for the QSAGE observations, resulted in 16 individual spectra per object.

An unavoidable feature of slitless spectroscopy is contamination from nearby sources. Despite the fact that this effect is substantially mitigated by the four independent grism orientations employed in the QSAGE survey, we nevertheless estimated the quantitative contamination for each individual spectrum. grizli initially generates models for each object in the catalogue assuming a linear continuum, based on their observed magnitudes. These models are then refined using a second-order polynomial fit directly to the observed spectra after subtracting off the initial contamination estimate. The contamination model of each spectrum can then be used to mask severely contaminated pixels when producing the final stacked spectrum across all orientations as discussed below.

Redshifts for sources in the grism spectra were primarily identified from the 1D spectra using a combination of Hα, Hβ, [O II], and [O III] emission features. Given the low-resolution nature of the grism spectra, significant blending of lines can occur, e.g. [O III] 4953 Å with [O III] 5007 Å and Hα 6562 Å with [N II] 6583 Å. In the higher signal-to-noise spectra these blends exhibit an asymmetry in the overall line profile, allowing (alongside the presence of Hβ emission) reliable differentiation between these lines. This asymmetry (and any Hβ emission) is often lost in lower signal-to-noise spectra and as such it can be difficult to differentiate between Hα at $z \sim 0.9$ and [O III] at $z \sim 1.6$. We therefore perform the line identification in two stages. First, lines are identified using an automatic fitting algorithm which then determines matches in wavelength ratios to common emission lines. We then visually inspect each spectrum, identify reliable detections, and attribute each detection a quality rating on a scale of $Q_w = 1$ to $Q_w = 4$ (where 4 represents a high S/N, multiple emission line detection and 1 represents a low-S/N less secure redshift). We mitigate the effect of contamination between nearby sources by simultaneously inspecting: a median stacked spectrum of all 16 exposures; the 4 separate median spectral stacks from the different roll-angle positions; and a mean-combination stack where contaminated pixels

in individual exposures are rejected based on the contamination model described above (see Fig. 3). Whilst the observations are most sensitive to detecting emission line objects at $z > 0.68$, in the absence of such emission lines, galaxies are also identifiable via absorption features and, at $z \gtrsim 2$, the 4000 Å break (examples of which are shown in Fig. 3).

We produce a catalogue of secure sources which require at least one of the following criteria to be met: multiple lines clearly observed in the grism spectrum; clearly asymmetric lines indicating blended [O III] emission or Hα/[N II] emission; or confirmed redshift from optical spectroscopy (i.e. VLT/MUSE data described below). The secure redshifts are used as a calibration/training set in our photometric redshift fitting analysis described below. With the photometric redshifts in hand, we then constrain the single blended emission line objects to the redshift most closely matched by the available photometric data. These objects are assigned a quality flag of $Q_w = 2$. For the subset of targets falling within the VLT/MUSE data field of view, we also use the optical spectra as a guide – both using the existence or the lack-of expected emission line features in the MUSE data to guide the identification of the grism data in this region.

We show the on-sky distribution of spectroscopically identified sources in Fig. 1, whilst example spectra from the grism data are shown in Fig. 3. The magnitude distribution of sources identified in the WFC3 G141 grism spectroscopy is given in the bottom panel of Fig. 4 and the redshift distribution is shown in Fig. 5.

2.3 VLT MUSE IFU spectroscopy

2.3.1 Overview and data reduction

The VLT/MUSE data for this field were taken as part of the Guaranteed Time MUSE Program (096.A-0222, PI: Schaye). MUSE provides IFU data across a 1 arcmin × 1 arcmin field of view, with a pixel scale of 0.2 arcsec pixel^{-1} (Bacon et al. 2010). All the observations were taken in the normal spectral mode with a wavelength coverage of 480–930 nm and resolution ranging from $R = 1770$ at the lower end of the wavelength range to $R = 3590$ at the higher end. A total of 12 exposures were taken, each of 900 s, totalling 3 h of integration on source. We have reduced the entirety of these data using the ESO MUSE pipeline (Weilbacher et al. 2014) with custom PYTHON scripts[2] (Fumagalli et al. 2014, 2017a) to optimize the illumination correction across different CCDs and using ZAP (Zürich Atmosphere Purge; Soto et al. 2016) to optimize the sky subtraction.

2.3.2 Source extraction and identification

Given the deep nature of the WFC3 NIR imaging, we use this as the basis for the source identification in the MUSE data. We first match the astrometry between the MUSE cube and the WFC3 *F*140*W* image (again using SCAMP, Bertin 2006) and then run SExtractor on the *F*140*W* image. From the resulting catalogue, we extract 1D spectra from the MUSE cube along with the variance and sky background measured for each spectrum. We use MARZ (Hinton et al. 2016) to measure redshifts from the spectra based on template fitting and visual inspection. For this we use A. Griffiths (September 2016) fork of the MARZ tool,[3] which includes templates covering redshifts up to $z \sim 6$ (for our wavelength coverage). Each identification is allocated a confidence flag, Q_m based on the following categorization:

(i) 1 – Low confidence/low S/N (can be single or multiple possible features);
(ii) 2 – Single line emitter, low-S/N continuum or continuum fit with weak or no emission lines;
(iii) 3 – Single line emitter, some hint of absorption lines in continuum or multiple emission lines with some at low signal-to-noise;
(iv) 4 – Multiple high-S/N emission and/or absorption lines;
(v) 6 – Star.

The single line emitters are predominantly [O II] emission at $0.88 \lesssim z \lesssim 1.5$ (which is partially resolved in the MUSE data) or Lyα at $z \gtrsim 2.9$ (which can be identified as such via asymmetries and continuum shape).

The magnitude distribution of sources in the MUSE field of view are shown in Fig. 4 (top panel). The pale blue circles show the total number of sources extracted from the WFC3 data in the MUSE field of view, whilst the dark blue circles show the magnitude distribution of sources identified with confidence flags of $Q_m = 2, 3, 4$, and 6. The spectroscopic identification is > 50 per cent complete up to $i < 25.8$ (where the *i*-band photometry is taken from the broad-band imaging described later). The redshift distribution of sources identified in the MUSE cube is given in the top panel of Fig. 5. The quasar redshift is marked by the vertical dashed line and coincides with an overdensity of [O II] emitting galaxies at $z \approx 1.4$. The redshift distribution appears to show some structure with a particular peak at the redshift of the QSO. For a detailed discussion of the QSO environments please see Stott et al. (in preparation).

Using the MUSE spectroscopic data, we are able to measure the accuracy of the WFC3 grism derived redshifts. The grism data are at a low resolution – $R = 130$, which equates to a rest-frame velocity uncertainty of ≈1000 km s^{-1} at $z \approx 1$. With a resolution of $R \approx 1800-3500$, MUSE has greater redshift accuracy (i.e. ≈50 km s^{-1} at $z \approx 1$), allowing a robust quantification of the grism line-fitting process's accuracy. A comparison of the redshifts determined using WFC3 and MUSE as a function of redshift is shown in Fig. 6, with $v_m - v_w$ giving the velocity offset between the MUSE and WFC3 redshifts in km s^{-1}. The dashed curves show the velocity uncertainty derived simply taking the G141 resolution limit of $R = 130$. From the 19 objects matched between the two samples, we find a velocity uncertainty on the G141 data of $\sigma_v = 680$ km s^{-1} (at $z = 1$). A closer inspection of the two outliers ($|\Delta v| > 2000$ km s^{-1}) shows that one is a very extended bright object, where the emission line is heavily 'smeared' in the grism spectrum due to the internal kinematics of the galaxy; whilst the second appears to be a statistical outlier due to spectral noise.

2.4 Optical imaging data

Supporting imaging is an important element in the analysis of the grism data, in particular in providing complementary photometric redshifts and galaxy properties. As described above, the photometric redshifts are needed for robust identification of objects detected with only single line features in the grism data. Below we describe the imaging datasets available on this field: (1) targeted William Herschel Telescope (WHT) auxiliary-port camera (ACAM) observations; and (2) coverage from the CFHTLS Wide-1 field.

[2] https://github.com/mifumagalli/mypython
[3] https://a-griffiths.github.io/Marz/

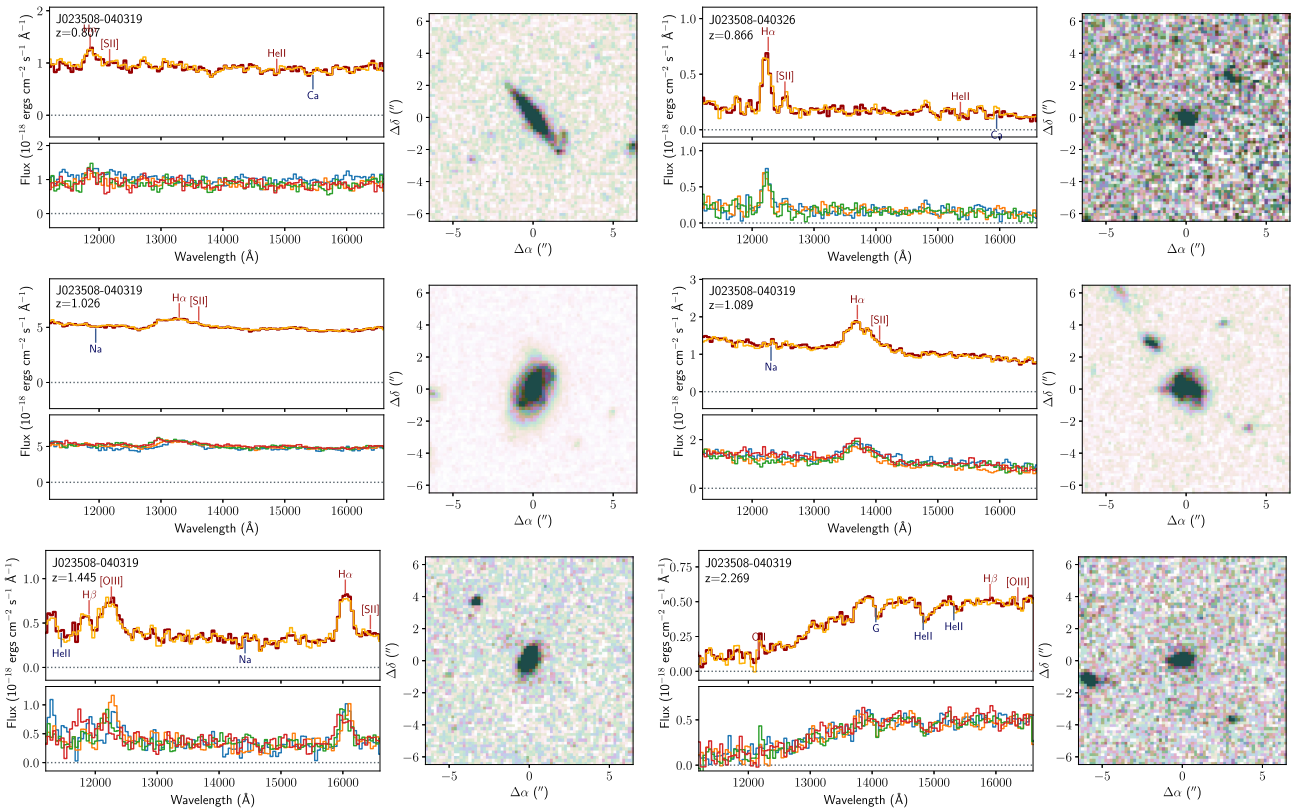

Figure 3. Example objects from the *HST* WFC3 grism data. In each case the top-left panel shows the median spectrum (orange) and contamination-masked mean spectrum (dark red). The lower-left panel in each case shows the corresponding spectra taken at each roll angle, whilst the right hand panel in each case shows a thumbnail taken from the WFC3 *F*140*W* stacked image.

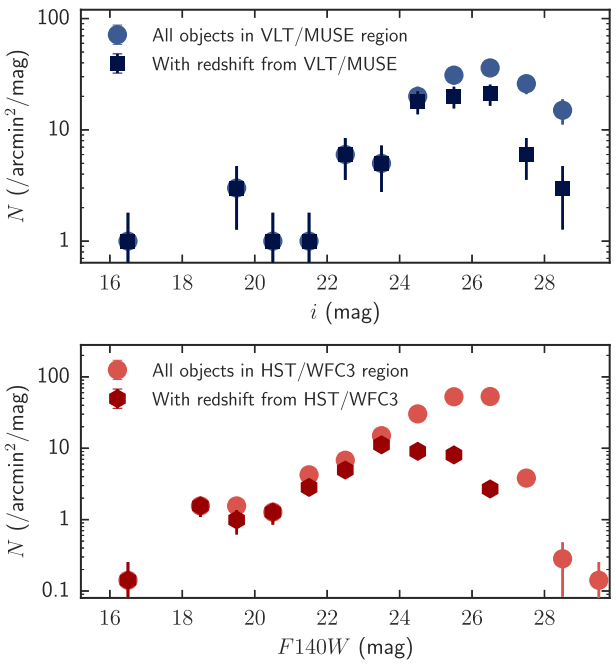

Figure 4. Magnitude distribution of sources in the MUSE (top panel) and WFC3 (lower panel) field of views. In both panels, the fainter circles denote number counts for all detected sources, whilst the darker circles show those with successfully identified redshifts from the MUSE and WFC3 grism spectroscopic data.

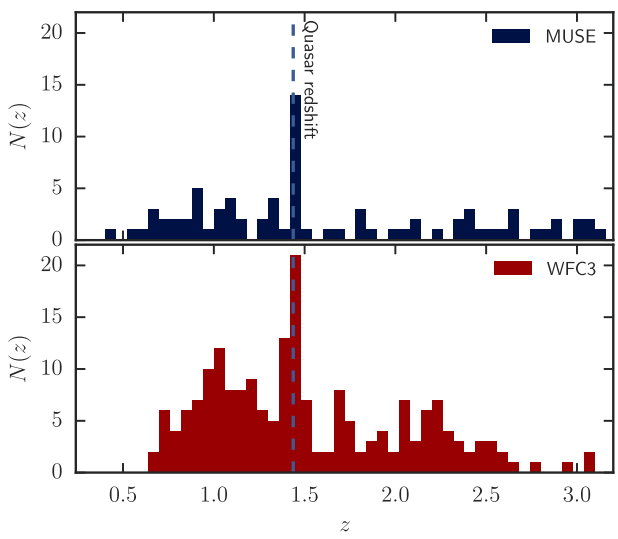

Figure 5. Redshift distribution of the MUSE spectroscopic redshifts (top panel) and the *HST*/WFC3 grism redshifts (lower panel). The vertical dashed line marks the redshift of the central quasar, PKS 0232−04.

2.4.1 *WHT ACAM*

The WHT ACAM imaging provides $i \sim 25$ mag depth imaging, with the SDSS *g*, *r*, and *i* filters. ACAM is mounted at the folded-Cassegrain of the WHT and covers a field of view with diameter $\oslash \approx 8$ arcmin at a pixel scale of 0.25 arcmin pixel^{-1}.

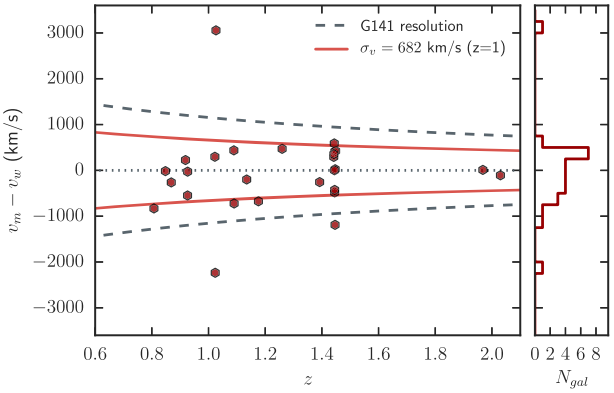

Figure 6. Rest-frame velocity offsets between redshifts for the same objects measured separately with VLT/MUSE and the *HST*/WFC3 G141 grism (red hexagons and histogram). The dashed curves denotes the rest-frame velocity scale given by $\pm c/R/(1+z)$, where $R = 130$ is the instrumental spectral resolution of the G141 grism. The achieved velocity accuracy of $\sigma_v = 682$ km s^{-1} (at $z = 1$) is represented by the solid red curves.

All observations were taken in observing runs W13BN5 (2013 November 24–25, PI: R. Crain), W14AN16 (2014 April 6–7, PI: R. Crain), and W17AP6 (2017 March 3–5, PI: R. Bielby). Seeing conditions were generally good with an image quality of ≈0.8–0.9 arcsec.

The ACAM data were reduced using standard image reduction methods. Master bias and flat-field frames were produced by stacking individual calibration frames, which were then applied to the science images. Individual weight maps for use with ASTROMATIC[4] software were produced from the flat-field images combined with a bad pixel mask. Astrometric solutions were derived for the images in each field using SCAMP and these were then used in constructing stacked images using SWARP.

Photometric calibration was performed by matching to the available (shallower) SDSS photometry in the region. Number counts for each of the filters are shown in Fig. 2 (dark blue squares), based on source catalogues extracted using SEXTRACTOR on the individual images. The corresponding depths, based on 80 per cent completeness of artificial point sources placed in the images, are given in Table 1.

2.4.2 *CFHTLS wide*

The central quasar studied here falls ≈3 arcmin from the Eastern edge of the CFHTLS (Cuillandre et al. 2012) W1 (wide) field (specifically in the 'W1.+4 + 3' region). The CFHTLS Wide survey provides relatively uniform imaging across a large area with the CFHLT *ugriz* filter set. Image quality is constrained to ≈0.9 arcsec across the survey, with the imaging reaching depths of $u, g, r, i \approx 25$ and $z \approx 24$ (AB), i.e. well suited to our needs. We note for reference that almost all of the W1 field has been surveyed spectroscopically to $i \approx 22.5$ as part of the VIPERS survey (Scodeggio et al. 2018), however the central quasar studied here lies marginally outside the extent of that survey (12 arcmin from the nearest VIPERS spectroscopic data point).

We downloaded the publicly available median stacked images for each of the five bands in W1.+4 + 3 from CADC (Canadian Astronomy Data Centre[5]). Using SCAMP, these were then matched to the WFC3 imaging astrometry and then resampled and cropped using SWarp to match the WFC3 stack field of view. The image seeing and 80 per cent point-source completeness levels are reproduced in Table 1 (taken directly from the CFHTLS synoptic table[6]). We show the number counts for objects detected in each of the bands across the WFC3-stack field of view in Fig. 2, based on catalogues extracted from the images using SEXTRACTOR.

2.5 Galaxy properties

2.5.1 *Collated photometric catalogue*

In addition to the individual *F*140*W* catalogue for grism extraction, we also produce a collated catalogue of all 10 ACAM, CFHTLS, and WFC3 filters. To do so, all images were astrometrically matched and resampled to a common grid using a combination of the SCAMP and SWARP software. SEXTRACTOR was then run in dual image mode using the *F*140*W* image as the detection image.

2.5.2 *Photometric redshifts*

Photometric redshifts are determined using the LE PHARE photometric fitting code (Arnouts et al. 1999; Ilbert et al. 2006), using the 'COSMOS' set of SED templates (as used by Ilbert et al. 2010). The template SED fitting was performed on all the available imaging data and using all secure spectroscopic galaxy redshifts from the MUSE IFU and WFC3 grism data (i.e. $Q_{w,m} = 3$ and $Q_{w,m} = 4$) as a training set. As discussed above, the photometric redshifts for the single line emitters with non-secure redshifts were then incorporated into optimizing the redshift identification for these objects.

A comparison between the LE PHARE photometric redshifts and the available spectroscopic data from WFC3 and MUSE is shown in Fig. 7 for magnitude limits of $i_{mag} < 24$, $i_{mag} < 25$ and $i_{mag} < 26$ (top, middle, and bottom panels, respectively). The red hexagons denote spectroscopic redshifts from WFC3, whilst the blue squares denote those from MUSE. In both cases, we only use those with confidence flags of 3 or 4 (given that objects with flags of 2 have partially been assigned redshifts with the photometric redshifts as a prior). Where an object is detected with both WFC3 and MUSE, we take the more accurate MUSE redshift. For each sample we quote the resultant photometric redshift accuracy, $\sigma_{z/(1+z)}$, and outlier percentage, η.

The photometric fitting shows reliable results at $i < 24$, with an accuracy of $\sigma_{z/(1+z)} = 0.053$ and an outlier rate of $\eta = 5.9$ per cent, whilst the results degrade at $i > 24$ as the photometric uncertainties increase. Evident from the comparison is a large scatter in the photometric redshift accuracy at $z = 1.44$. These are galaxies in the local environment of the bright QSO, many of which appear to have spectral line ratios indicative of significant active galactic nucleus (AGN) activity (which we investigate further in a forthcoming paper). Whilst these specific objects have little impact on the intervening absorber science in this paper, we note that any AGN in the foreground of the QSO will have accurate spectroscopic redshifts from their strong line features. We note that the varying image quality across the imaging bands could cause issues for the photometric fitting, this is countered to some degree by the adaptive fitting incorporating the spectroscopic training set, which

[4] https://www.astromatic.net/

[5] http://www.cadc-ccda.hia-iha.nrc-cnrc.gc.ca/

[6] http://terapix.iap.fr/cplt/T0007/table_syn_T0007.html

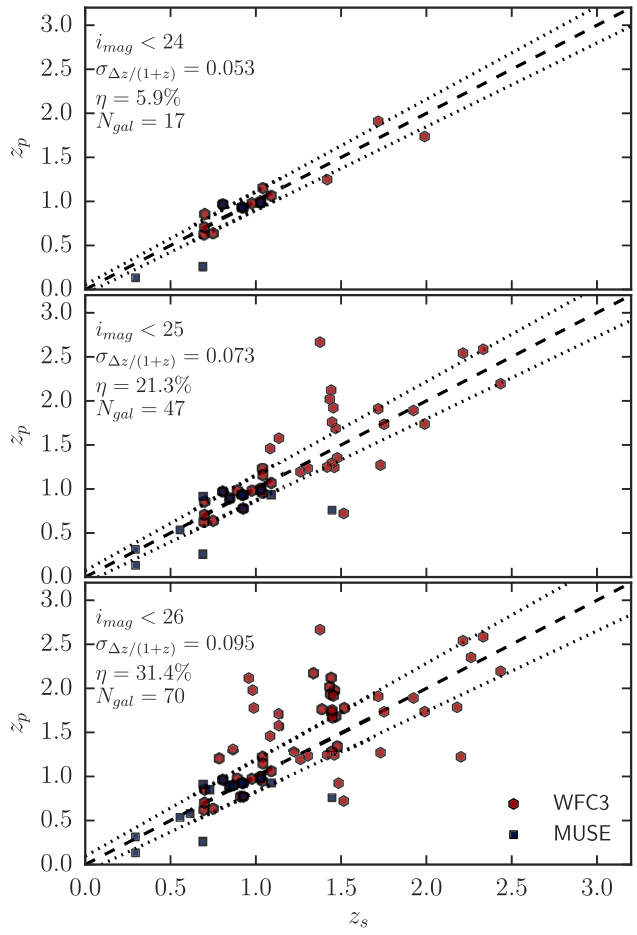

Figure 7. Photometric (z_p) versus spectroscopic (z_s) redshifts for all galaxies identified with confidence $Q_{op} = 3$ or $Q_{op} = 4$ in the *HST*/WFC3 grism (red hexagon points) or the VLT/MUSE (blue square points) data. The dashed line shows $z_p = z_s$ and the dotted lines show the 1σ on the distribution of $(z_p - z_s)/(1 + z_s)$.

determines and applies constant offsets (of $\Delta m \lesssim 0.1$) to the input photometry.

2.5.3 Star formation rates

Over the main redshift range of interest ($0.68 < z < 1.44$), we primarily use the Hα fluxes measured from the grism data to estimate SFRs for the individual galaxies in our sample. Using the relation given in Kennicutt (1998), divided by a factor of 1.8 to convert from Salpeter to Chabrier IMF. The galaxy intrinsic Hα luminosities are estimated using an extinction correction of $A_{\mathrm{H}\alpha} = 0.818A_V$ (Cardelli, Clayton & Mathis 1989), where we use a value of $A_V = 1$ (consistent with the mean absorption estimated from the template fitting with LE PHARE and with Garn & Best 2010 for galaxies of mass $M_\star \approx 10^{9.5-10}$ M$_\odot$). We remove the estimated [N II] contribution to the blended Hα-[N II] emission assuming $\log([\mathrm{N\,II}]/\mathrm{H}\alpha) = -1.0$ (Faisst et al. 2018).

We supplement the Hα derived SFRs with [O II] SFR estimates where [O II] emission is observed either in the grism data or the MUSE data. SFRs are estimated from the [O II] fluxes based on the relationship given by Kennicutt (1998) adapted for the non-local galaxy population by Kewley, Geller & Jansen (2004) and using $A_V = 1$ and $A_{[\mathrm{O\,II}]} = 1.54A_V$ based on Cardelli et al. (1989). We note that for the objects where both [O II] and Hα are detected, we find the two indicators give broadly consistent measures of the SFR (with an average offset of ≈0.03 dex and a scatter of ≈0.4 dex). In these instances, where we have both [O II] and Hα measures of the SFR, we favour the Hα for the analyses presented here given that it will be less affected by extinction and have a lesser dependence on metallicity and ionization parameter (e.g. Kewley et al. 2004; Gilbank et al. 2010). The resulting galaxy SFRs are given as a function of redshift in the upper-left panel of Fig. 8. We find a Hα-derived SFR systematic lower limit in the primary redshift range of interest in this study (i.e. $0.68 < z < 1.44$) of ≈0.2–0.8 M$_\odot$ yr^{-1}. For galaxies with upper limits on the Hα and/or [O II] fluxes, we propagate these upper limits to determine upper limits on the SFR.

2.5.4 Galaxy stellar masses

Given the catalogue of spectroscopic and photometric redshifts for our sample, we next derive galaxy stellar masses also using LE PHARE (via the GAZPAR online interface[7]). Following Ilbert et al. (2010), we use a set of SED templates calculated using the stellar population synthesis models of Bruzual & Charlot (2003). We assume a Chabrier (2003) IMF and an exponentially declining star formation history. Dust extinction is then applied to the templates using the Calzetti et al. (2000) law, with $E(B - V)$ in the range 0–0.7.

Stellar masses for the spectroscopically identified galaxy sample are given in the lower-left panel of Fig. 8. The depths of our NIR imaging correspond to approximate limiting masses of $M_\star \approx 10^{7.5-8}$ M$_\odot$ across the redshift range $0.68 < z < 1.44$. In the right-hand panels of Fig. 8 we show the SFR and sSFR versus stellar mass for the galaxy sample in the redshift range $0.68 < z < 1.44$. Points are colour-coded by each galaxy's redshift. For comparison, the plotted line shows the $z \approx 1$ star formation main-sequence trend reported by Karim et al. (2011). From this, we can see that the galaxies lie on or around the star-forming main sequence.

2.5.5 Inferred galaxy halo properties

Based on the derived stellar masses, we infer galaxy halo masses (M_{halo}), virial radii (R_{vir}), virial velocity dispersions (σ_{v}), and virial temperatures (T_{vir}) estimates for each of our galaxies. Clustering studies suggest a correlation between galaxy stellar mass and host halo mass over a wide range of redshift based on the ΛCDM prediction of distribution of dark matter (e.g. Wake et al. 2011; Coupon et al. 2012; Bielby et al. 2014; Cochrane et al. 2018). Here we infer halo masses based on the individual estimated stellar masses of the galaxies in our sample using the relations based on abundance matching presented by Behroozi, Wechsler & Conroy (2013). From these halo masses, we then (with a number of simplifying assumptions) infer virial radii and virial temperatures for these structures (e.g. Shull 2014; van de Voort 2017). The virial radius for a given halo mass can be expressed as

$$R_{\mathrm{vir}} \approx 340\mathrm{kpc} \left(\frac{M_{\mathrm{halo}}}{10^{12}\mathrm{M}_\odot} \right)^{\frac{1}{3}} \frac{1}{1+z} \quad (1)$$

using a 'virial overdensity' threshold of $18\pi^2$ (e.g. Bryan & Norman 1998; van de Voort 2017). The halo velocity dispersion, σ_{v} is

[7] https://gazpar.lam.fr

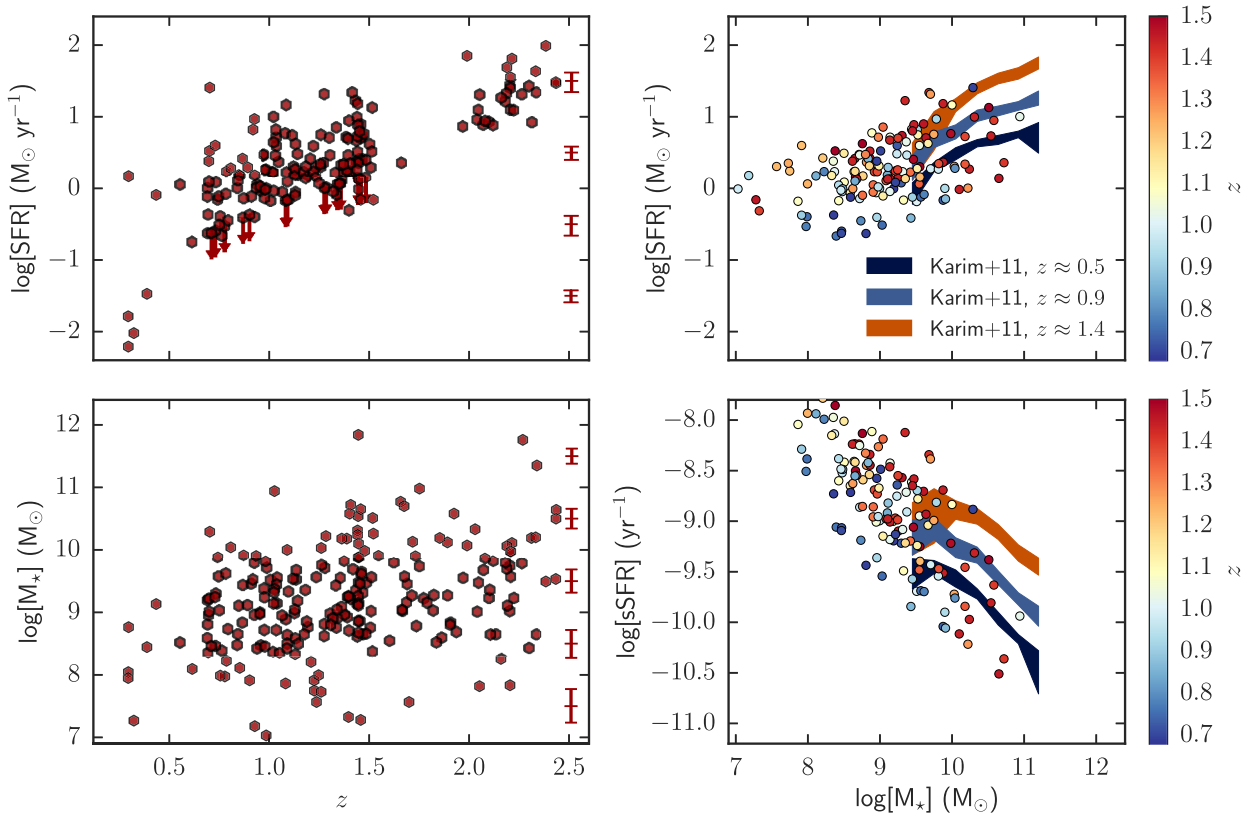

Figure 8. Derived photometric properties of the spectroscopically identified galaxy sample. SFRs were estimated primarily from measured Hα emission where available and [O II] where Hα was not covered by the spectral range of the data. Galaxy masses were estimated using photometric fitting to the available photometric data. The error bars along the right-hand axes of the left-hand panels show the mean estimated uncertainty on the points in bins of 1 dex. In the right-hand panels we limit the data to the prime redshift range of interest ($0.68 < z < 1.4$) and colour code points by redshift (as defined by the associated colour-bars). For reference, we also show the $M_\star$−SFR relations derived at $z \approx 0.5$, $z \approx 0.9$, and $z \approx 1.4$ given by Karim et al. (2011) (solid curves colour-coded by redshift, with the line widths indicating the uncertainties on the mean SFR measurements).

estimated using the above halo mass and virial radius, whilst the corresponding virial temperature can be expressed as

$$T_{\rm vir} \approx 3 \times 10^5 \,{\rm K} \left(\frac{M_{\rm halo}}{10^{12} {\rm M}_\odot} \right)^{\frac{2}{3}} (1+z) \qquad (2)$$

assuming a mean molecular mass of $\mu = 0.59$ (e.g. van de Voort 2017). We make a note of caution that the environments in which a number of the galaxies in our survey exist are perhaps unlikely to be virialized. It is with this caveat that we use the virial radius in this work, and as such use such a metric largely to give a relative sense of scale between different galaxies within our study. For context, at $R_{\rm vir}$ (for $M_{\rm halo} \approx 10^{12}$ M$_\odot$ at $z \approx 1$) the escape velocity is $v_{\rm esc} \approx 260$ km s^{-1}, whilst at $2R_{\rm vir}$ the escape velocity is $v_{\rm esc} \approx 180$ km s^{-1}.

2.6 High-resolution ultraviolet absorption spectroscopy

The *HST* spectroscopic observations with COS were obtained as part of the COS Absorption Survey of Baryon Harbors (CASBaH, *HST* Programs 11741 and 13846, PI: T. Tripp). Full details about the CASBaH programme design and data handling are reported by Tripp et al. (in preparation); here we briefly summarize some important aspects of the data set. CASBaH was designed to obtain high-resolution spectra with complete coverage from observed wavelength $\lambda_{\rm ob} = 1150$ Å to the redshifted wavelength of the Lyα emission line of each target QSO. This was achieved using the far-UV G130M and G160M COS gratings (resolving power $R =$ 18 000−22 000 or FWHM ≈15 km s^{-1}), the near-UV COS G185M and G225M gratings ($R =$ 16 000−24 000; Osterman et al. 2011; Green et al. 2012), and the STIS E230M echelle spectrograph ($R =$ 30000; Kimble et al. 1998; Riley et al. 2018; Woodgate et al. 1998). Table 2 provides a log of the COS and STIS observations.[8]

The FUV G130M and G160M spectra were obtained to survey very weak absorption lines such as the Ne VIII doublet and

Table 2. Ultraviolet spectroscopy of PKS 0232−042 with *HST*.

Instrument/ grating	Observation date	Exp. time (ks)	*HST* programme (PI)
COS/G130M	2010 Feb.	16.019	11741 (Tripp)
COS/G160M	2010 Jan.	22.841	11741
	2010 Feb.		
COS/G185M	2015 July	23.424	13846 (Tripp)
COS/G225M	2015 July	29.060	13846
	2015 Aug.		
STIS/E230M	2001 Feb.	41.934	8673 (Jannuzi)
	2002 Jan.		

[8]For further information about the design and performance of COS, please see Green et al. (2012) and Osterman et al. (2011). Information about the design and performance of STIS can be found in Woodgate et al. (1998), Kimble et al. (1998), and Riley et al. (2018).

accordingly required higher signal-to-noise (S/N) ratios. The NUV were obtained to record the stronger H I and longer-wavelength metal species (e.g. C III, Si III, and O VI) affiliated with Ne VIII absorbers; for the detection of these stronger lines, lower S/N was acceptable. For PKS 0232−042, the COS G130M and G160M spectra have median S/N ratios of 13 and 17, respectively, whilst the COS G185M and G225M spectra have median S/N = 5. The STIS E230M spectrum has median S/N = 7.

We reduced the FUV data as described in Meiring et al. (2011) and Tripp et al. (in preparation). In brief, we used the CALCOS pipeline (version 3.1.7) to carry out the initial reduction steps leading to one-dimensional extractions of the spectra from the individual exposures, and we aligned the individual exposures by comparing the positions of well-detected lines with distinctive component structure. COS employs a photon-counting detector with very low backgrounds, so we next coadded the individual exposures to accumulate the total gross and background counts in each pixel, which we used to determine the uncertainty in the flux based on counting statistics. For this absorption study, the absolute flux of the QSO is irrelevant, so no absolute flux calibrations were applied to the FUV spectra. The COS pipeline produces highly oversampled data, so we also binned the spectra to two pixels per resolution element to optimally sample the spectra. For the NUV COS and STIS data, we similarly used CALCOS and CALSTIS (v. 2.22) to extract 1D spectra. However, for these data it was more convenient to flux calibrate the data (e.g. to account for the echelle blaze function of STIS), and then we aligned and coadded the individual spectra with the weighting method described by Tripp et al. (2001).

Absorption lines in the PKS 0232−042 spectrum were identified by inspecting every single line in the spectrum in many ways with a variety of tools. For every line, we checked whether the line would be an O VI candidate based on the velocity spacing and relative strength of the O VI doublet. This search for O VI did *not* require that H I is detected or not; we only searched for two lines with the signature spacings of O VI. Interestingly, detection of O VI without HI mainly occurs in absorbers with $z_{\rm abs} \approx z_{\rm quasar}$, i.e. this seems to be a signature of ejected or at least 'proximate' absorption systems (Tripp et al. 2008). Examples of individual O VI *components* in intervening absorbers without H I at the same velocity can be found in Tripp et al. (2008) and Savage et al. (2010). However, in these examples, H I is clearly detected in other components of the same absorption systems. We corroborated the line identifications by searching for H I and other metal lines detected in the O VI absorption systems. Affiliated metals and H I lines often have similar (or identical) component structure as the O VI absorption profiles (Tripp et al. 2006, 2008, 2011), which gives additional credence to the identifications. Information on the other lines detected in these systems can be found in Tripp et al. (in preparation). Note that Tripp et al. (in preparation) provide information on additional, weaker O VI candidates; in this paper we concentrate on the well-detected O VI systems recorded at high significance (with upper limits used in place of the low-confidence weak lines).

Using the Voigt-profile fitting software developed by Burchett et al. (2015), we fitted multicomponent absorption-profile models to constrain the column density ($N_{\rm O\,VI}$), velocity width (b), and velocity centroid of each component, and for purposes of comparison, these Voigt-profile parameters were used to calculate the equivalent width of each component using a full curve of growth. We use the convention of Tripp et al. (2008), i.e. we use the velocity centroid of the strongest O VI component to define the systemic redshift of the absorber. The resulting measurements for each O VI absorption doublet are given in Table 3. In general, we fit all available resonance transitions of a specific species simultaneously (e.g. the O VI 1031.93 and 1037.62 Å lines are fitted jointly and must have the same parameters), but different species are fitted independently (e.g. the H I profile parameters are entirely independent of the O VI parameters). We do not attempt to extract information about turbulent versus thermal broadening of the lines in this paper. In some instances, the O VI (or other) lines of interest are blended with interloping lines from other redshifts. In these cases, we include the interloping lines in the fit, but again, the interloper parameters are allowed to freely vary and are entirely independent of the parameters of the target O VI lines. Because the CASBaH data have broad wavelength coverage extending from 1152 Å to the Ly α emission line of the QSO, the interloping lines are often well constrained by other lines in the CASBaH data. For example, the O VI 1031.93 Å line at $z = 0.173\,55$ is blended with an H I 915.82 Å line at $z = 0.322\,50$; the parameters of this interloper are tightly constrained because many other H I Lyman series lines at this redshift are recorded in the CASBaH data, and those other Lyman lines are included in the overall fit.

We show the absorption systems, and the associated model fits, used in this paper in Fig. 9. In each panel, the black line shows the entire Voigt-profile model including all blends that were included in the fit, and the red line shows the Voigt-profile model for only the species of interest (indicated in each panel). We show three panels per absorption system: one of the H I Lyman series lines (often there are many to choose from; we selected the one that was most informative, but all available Lyman series lines were used in the fit); and both of the lines of the O VI doublet. Whilst we are only studying O VI in this paper, it is helpful to see the corresponding H I to corroborate the O VI identification. Tripp et al. (in preparation) gives the full suite of lines detected and measured in each of these systems. Note that for the O VI absorber at $z_{\rm abs} = 0.173\,55$, the O VI 1038 Å line is lost in the Milky Way Ly α + geocoronal Ly α

Table 3. Parameters for the identified O VI doublet absorption systems found in the PKS 0232−04 sightline using the *HST* COS and STIS data.

z_{sys}	Δv (km s^{-1})	EW (Å)	log[N(O VI]) (cm^{-2})	b (km s^{-1})
0.173 55	+0 ± 4	0.54	13.7 ± 0.1	18.9 ± 6.5
0.218 02	−67 ± 8	0.64	13.8 ± 0.1	34.8 ± 11.1
	+0 ± 1	1.87	14.5 ± 0.1	23.9 ± 2.2
	+74 ± 2	1.04	14.0 ± 0.1	25.1 ± 3.1
0.322 43	+0 ± 4	0.59	13.7 ± 0.1	33.4 ± 6.1
0.355 89	+0 ± 6	0.33	13.5 ± 0.1	24.3 ± 9.2
0.363 84	−87 ± 12	0.36	13.5 ± 0.1	42.4 ± 20.3
	+0 ± 5	0.54	13.7 ± 0.1	21.5 ± 7.1
	+76 ± 2	0.35	13.5 ± 0.1	10.9 ± 4.8
0.434 31	−81 ± 3	0.77	13.9 ± 0.1	30.4 ± 4.6
	+0 ± 2	0.69	13.9 ± 0.1	14.8 ± 3.2
0.512 08	−95 ± 4	0.32	13.5 ± 0.1	14.2 ± 6.2
	+0 ± 6	0.39	13.5 ± 0.1	25.7 ± 8.6
0.739 01	−189 ± 23	1.07	14.0 ± 0.2	63.1 ± 32.9
	+0 ± 8	2.54	14.4 ± 0.1	73.3 ± 11.7
0.807 83	−167 ± 4	0.88	14.0 ± 0.1	16.8 ± 6.4
	+0 ± 3	2.65	14.6 ± 0.1	32.9 ± 4.3
0.868 16	−52 ± 10	0.28	13.4 ± 0.4	9.9 ± 17.0
	+0 ± 4	1.77	14.4 ± 0.1	22.6 ± 6.3
1.088 94	+0 ± 13	2.09	14.4 ± 0.2	31.6 ± 13.9
	+66 ± 40	0.87	13.9 ± 0.6	34.2 ± 45.7
1.356 46	−45 ± 25	0.92	14.0 ± 0.4	29.2 ± 28.9
	+0 ± 8	1.13	14.1 ± 0.3	18.4 ± 9.5

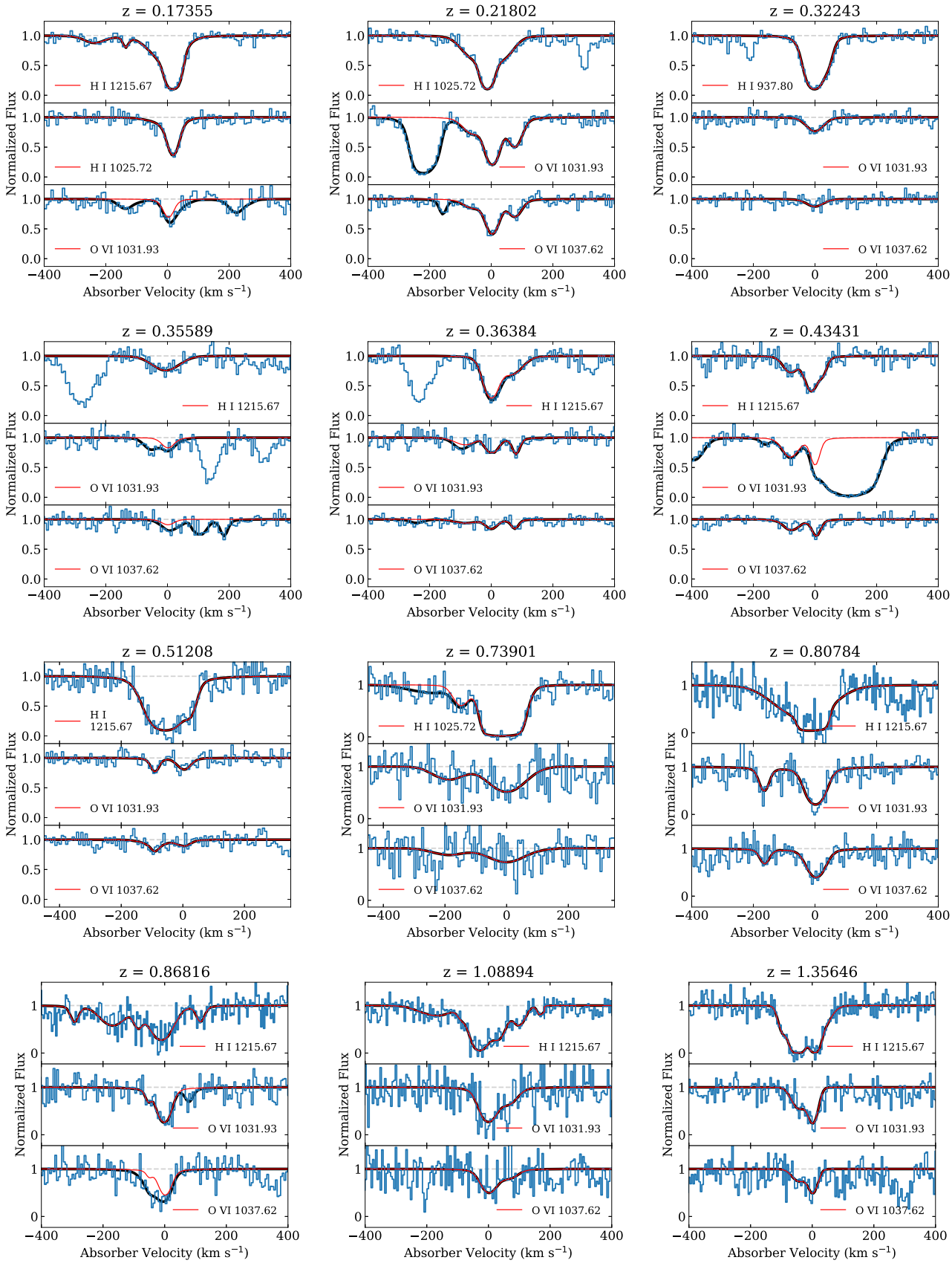

Figure 9. Spectra (blue step histogram) of O VI and H I absorption lines (as labelled) overlayed with the absorption-profile fits. In each panel, the black line shows the full fit (including blends from interloping lines from other redshifts), and the red line shows the Voigt-profile model for the O VI or H I only.

complex, so we do not show the 1038 Å data in that stack. Instead, we show the Ly α, Ly β, and O VI 1032 Å lines.

3 THE GALAXY ENVIRONMENT OF O VI ABSORBERS

The blind nature of both the *HST*-WFC3 grism and VLT-MUSE large field IFU data provide a large quantity of information on the galaxy environment directly surrounding the gaseous environments probed along the quasar sightline. We aim to utilize these data to probe the galaxy environments of the individual O VI absorption systems along the line of sight.

We consider the systems in two separate redshift ranges: i.e. a low-redshift sample (i.e. $z < 0.68$), where the galaxy population is primarily probed up to ≈0.5 arcmin from the sightline by the MUSE data; and a high-redshift sample ($0.68 < z < 1.44$), where the population is revealed over a wider field of view up to ≈1.5 arcmin with the grism data. For the analyses that follow, we define a velocity window within which to consider an absorber to be associated with a local galaxy. We consider a number of physical factors: (1) the rotational velocity of galaxies within the mass range covered by our sample; (2) the typical range of velocities measured for outflowing material from galaxies; (3) the velocity dispersion of galaxies within galaxy groups and clusters; and (4) the velocity uncertainties on the galaxy redshifts themselves.

Taking typical galaxy rotation curves for guidance, galaxies at $z \approx 1$ with masses of $\approx 10^{10}$ M$_\odot$ have median rotational velocities of ≈120–160 km s^{-1}, although rotational velocities of up to ≈2 × the median are common (e.g. Johnson et al. 2018). Velocity offsets of up to ≈320 km s^{-1} therefore seem reasonable if any O VI absorption is tracing co-rotating material within the galaxy halo. Considering galactic winds driven by star formation activity, outflow velocities of $v_w \approx$ 200–400 km s^{-1} are typical at the redshifts we probe (e.g. Mathes et al. 2014), although wind velocities of up to ≈600 km s^{-1} have also been reported (e.g. Shopbell & Bland-Hawthorn 1998; Shapley et al. 2003; Tripp et al. 2011). In terms of large-scale galaxy structures, massive galaxy clusters can have velocity dispersions up to ≈1000 km s^{-1} (e.g. Struble & Rood 1999). Such a large velocity window is clearly not appropriate for draw associations with the average galaxy population, however, so such a large offset will only be considered in this work where a galaxy group or cluster is detected. Allowing for the potential range in velocity offsets, we set a velocity window for associating absorbers with galaxies of $\Delta v_{\rm max} = \max\{400\,{\rm km\,s^{-1}}, \sigma_v\}$, where σ_v is the velocity uncertainty on any given galaxy (i.e. ≈50–80 km s^{-1} for galaxies with MUSE redshifts and ≈682 km s^{-1} for galaxies with only grism redshifts). As a reference point, low redshift studies (Werk et al. 2016; Nielsen et al. 2017; Kacprzak et al. 2019) find O VI absorber–galaxy pairs, at $z = 0.2$, associated in velocity space within $|\Delta v| \lesssim 200$ km s^{-1}.

In the following section, we provide details of individual absorber–galaxy associations, discussing system properties and environment on a case-by-case basis. We collate the data and present the statistical properties of the sample as a whole in Section 3.2.

3.1 Census of O VI systems

An overview of the field is presented in Fig. 10, where all detected O VI absorbers (diamonds) and galaxies (squares and hexagons) at $z < 1.5$ are shown as a function of redshift and impact parameter to the quasar sightline (lower panel). The top panel shows a histogram of the galaxy population within 600 kpc of the sightline at $0.68 < z < 1.44$. The vertical shaded regions highlight redshifts coincident with the O VI absorbers. The dotted and dashed horizontal lines in the top panel denote the median and twice the median galaxy density in the field, respectively. The data reveal a diversity of environments in terms of galaxy density and potential associations between O VI absorption systems and the galaxy population.

We now look at how the ionized oxygen is distributed around the galaxies, by analysing the column density of O VI absorbers as a function of impact parameter to individual detected galaxies within our given $\Delta v_{\rm max}$ constraints. This is shown in Fig. 11, where the filled red hexagons and dark blue squares denote the QSAGE O VI–galaxy pairs at $z > 0.68$ and $z \leq 0.68$, respectively. We differentiate upper limits as pale hexagons and squares for the two samples respectively. These upper limits are calculated within $\Delta v \leq 50$ km s^{-1} of detected galaxies in the survey sample. The open hexagons show the impact parameters of galaxies that are not the nearest to the sightline, but do fall within the $\Delta v_{\rm max}$ velocity window. We find five O VI absorption systems associated with galaxies in our sample at $z > 0.68$ and a further three at $z \leq 0.68$, given the $\Delta v_{\rm max}$ constraint on associations. These fall primarily at impact parameters of ≈100 kpc, but extend to ≈350 kpc in the most extreme case. Within this range in impact parameters, we found numerous non-detections with limits of $N_{\rm O\,VI} \lesssim 10^{13.5\text{–}14}$ cm^{-2}. These non-detections point to a large scatter in O VI column densities within ≈300 kpc of galaxies at $z \sim 1$.

For comparison, we also show the COS-Haloes measurements taken from Werk et al. (2016, green points). The triangle, diamond, and circle points show broad, narrow, and 'no low-ionization' absorbers, respectively. The Werk et al. (2016) data consist primarily of isolated galaxies at $z < 0.2$, with impact parameters of $\lesssim$120 kpc ($\lesssim 0.9\,R_{vir}$) and $M_\star \gtrsim 10^{9.6}$ M$_\odot$. The blue '+' symbols show the results of Kacprzak et al. (2015). These show isolated galaxies probing down to a faintest galaxy near-infrared (AB) magnitude of ≈22.5 mag (corresponding to a minimum stellar mass of $\approx 10^8$ M$_\odot$). We estimate these data probe up to a maximum impact parameter in units of the virial radius of $b/R_{\rm vir} \approx 1.8$. Complementary to these, the orange '×' symbols show column densities from Pointon et al. (2017), which correspond to galaxies identified to be in groups at $z < 0.5$. In collating these datasets, we only plot points for the galaxies that are deemed to be 'associated' with each individual absorber by the corresponding authors (i.e. we do not plot multiple galaxies for a single absorber). Combining these datasets here produces a broad mixture of galaxy properties and environments, such that caution is required in comparing any one sample to another. However, noting this, our own sample is effectively a blind selection incorporating whatever environments and galaxies happen to be found along the given sightline.

The dashed curve and shaded region show a fit calculated by Werk et al. (2016) for their broad absorber (triangle) data. The distinction between the broad and narrow categories here is identified using the Doppler parameter at a value of $b \sim 30$ km s^{-1}. Werk et al. (2016) exclude narrow O VI absorption and absorbers with no associated low-ionization lines from this fit to the data, finding that these dominate the large scatter in the observed column densities. Quantitatively, 15 out of 16 of the Werk et al. (2016) broad absorbers lie on the relation, whilst 13 of 17 narrow and 'no-low' absorbers deviate significantly below the fit. Two of our own data points at $z < 0.68$ lie at impact parameters, both in proper distance and as a fraction of virial radius ($r_{\rm vir}$), approximately equivalent to the Werk et al. (2016) data. These both lie well below the $z \sim 0.2$ broad-absorber fit and are more consistent with the narrow absorbers of Werk et al. (2016). Indeed both have velocity widths

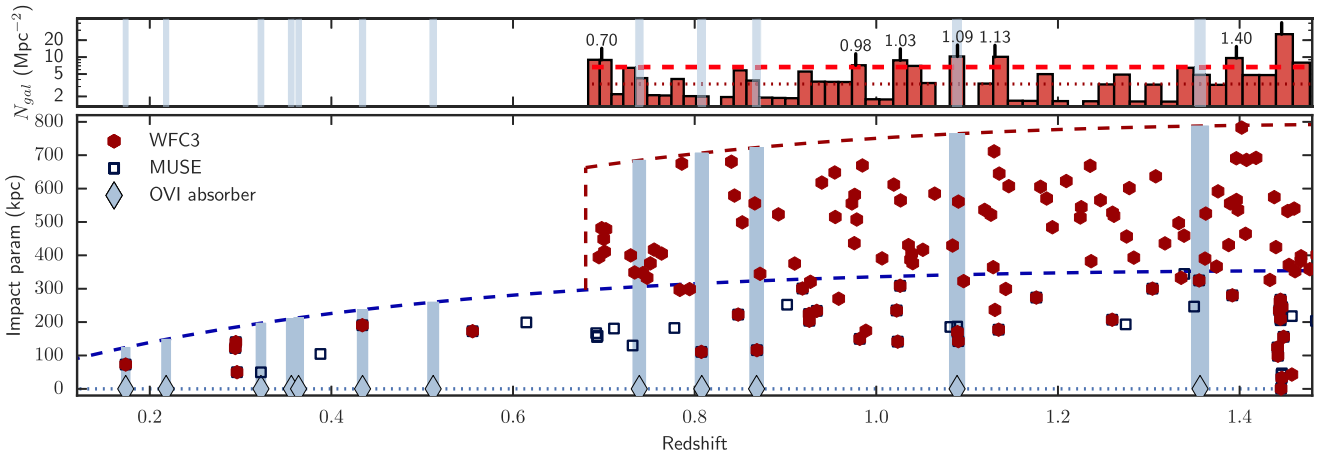

Figure 10. Redshift versus impact parameter for all identified galaxies within the MUSE (inner dashed curve) and WFC3 grism (outer dashed curve) fields of view. O VI absorbers along the quasar sightline are marked by the shaded regions with ±1000 km s^{-1} intervals to highlight any potentially associated galaxies or galaxy structures. The galaxy number density within $\Delta v \pm 100$ km s^{-1} bins (histogram) alongside the O VI absorber positions. The horizontal dashed line shows the median observed galaxy density in the WFC3 grism field of view (within the redshift range $0.68 < z < 1.38$). The O VI absorbers are found in a range of galaxy environments, with at least one out of the five coinciding with a potential group environment (i.e. twice the mean density as given in the text) and two having no associated galaxy within 200 kpc (although all have associated galaxies within ≈350 kpc).

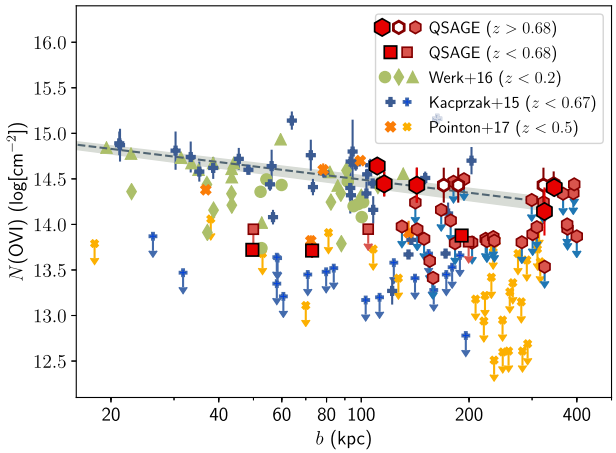

Figure 11. O VI column density as a function of impact parameter. The low-redshift ($z < 0.68$) points from our dataset are shown by the blue squares, whilst the red hexagons denote the $0.68 < z < 1.44$ sample (in both cases, the paler symbols denote upper limits). The open symbols show galaxies coincident with a detected absorber, where a galaxy at smaller impact parameters is also present. Data points from Kacprzak et al. (2015) and Pointon et al. (2017) are shown by the blue plus and orange times symbols, respectively. The data of Werk et al. (2016) are shown by the green triangles, diamonds, and circles (denoting broad, narrow, and no low-ionization subsets). The dashed curve and shaded region show a fit to the Werk et al. (2016) broad absorbers (extrapolated to larger impact parameters).

of $b \lesssim 30$ km s^{-1}, chosen by Werk et al. (2016) to classify between broad and narrow absorption systems. The third galaxy-absorber pair similarly corresponds to a narrow absorption feature and lies significantly below the Werk et al. (2016) fit to the column densities of broad absorbers extrapolated to impact parameters beyond the range of their data.

Considering the $0.68 < z < 1.4$ absorber–galaxy pairs from our data, these generally lie at impact parameters extending beyond the range of the Werk et al. (2016) data, whilst also representing galaxies of different masses, SFRs and environments. Despite these caveats, the detections at $z > 0.68$ in our own data (which are predominantly $b \gtrsim 30$ km s^{-1} absorbers) are consistent with the extrapolated low-redshift fit, suggesting some consistency between the picture at $z < 0.2$ and at $z \sim 1$. The extent to which we identify absorbers at distances of up to $b \approx 300$–400 kpc (or $b \approx 4$–$5R_{\rm vir}$) from the most proximate detected galaxy appears comparable to wide field low-redshift results such as those presented by Mathes et al. (2014), Kacprzak et al. (2015), Johnson, Chen & Mulchaey (2015a), and Pointon et al. (2017).

We now consider individual systems of interest: (1) those where O VI is detected; (2) those where a galaxy or set of galaxies falls within $b \lesssim 2R_{\rm vir}$ of the quasar sightline but no O VI is detected; or (3) a candidate group/cluster environment is found within the WFC3 data field of view. In this instance, we focus on galaxies within impact parameter $b/R_{\rm vir} = 2$ cut prompted in part by results at low redshift (Tumlinson et al. 2011; Shull 2014) but also for brevity in focusing on only the systems of most interest where we might have expected to find absorption systems based on previous studies. We provide a list of the proximate galaxies along the sightline and their properties in Table 4.

3.1.1 Absorbers at $z < 0.68$

Whilst the data at $z < 0.68$ do not probe the large physical scales afforded by the higher redshift sample, we do detect a number of galaxies coincident with absorbers in the sightline. These are shown in Fig. 12 alongside all $z < 0.68$ galaxies that lie within $b = 2R_{\rm vir}$ where no O VI absorption is detected.

The absorbers at $z = 0.1736$, $z = 0.3224$, and $z = 0.4343$ are all found to lie within $2R_{\rm vir}$ of galaxies detected in the MUSE data. The velocity offsets between the galaxies and absorbers in all three cases are $\lesssim 50$ km s^{-1}, i.e. relatively small in comparison to the nominal halo σ_v estimates for the galaxies ($\gtrsim 200$ km s^{-1}). We note that the absorbers detected at $z = 0.218$, $z = 0.356$, $z = 0.364$, and $z = 0.512$ show no detected galaxies in the deep MUSE data within a few 1000 km s^{-1} and therefore are not shown in Fig. 12. The MUSE field of view at these redshifts corresponds to maximum probed impact parameters of $b = 109$ kpc (compared to a virial radius of

Table 4. Properties of proximate galaxies to the quasar sightline. First five lines shown only, full table available online.

ID	RA (J2000)	Dec.	m_{F140W} (AB)	z	b (kpc)	$\log(M_\star)$ ($M_\odot$)	$\log(M_{\rm halo})$ ($M_\odot$)	$R_{\rm vir}$ (kpc)	log(SFR) ($M_\odot$ yr^{-1})
QSAGE J023508.12+023508.1	38.78385	−4.04062	19.41 ± 0.01	0.1735	73	$9.45^{+0.01}_{-0.01}$	$11.5^{+0.1}_{-0.1}$	148^{+23}_{-23}	$-0.25^{+0.01}_{-0.01}$
QSAGE J023506.49+023506.5	38.77705	−4.02821	23.79 ± 0.05	0.2942	122	$7.95^{+0.21}_{-0.19}$	$10.6^{+0.2}_{-0.2}$	63^{+41}_{-38}	$-1.79^{+0.07}_{-0.08}$
QSAGE J023506.12+023506.1	38.77551	−4.02791	23.06 ± 0.01	0.2948	140	$8.04^{+0.01}_{-0.01}$	$10.6^{+0.1}_{-0.1}$	66^{+10}_{-10}	$-2.21^{+0.08}_{-0.10}$
QSAGE J023507.78+023507.8	38.78240	−4.03727	22.63 ± 0.02	0.2961	50	$8.76^{+0.08}_{-0.16}$	$11.2^{+0.1}_{-0.2}$	101^{+26}_{-48}	$0.17^{+0.09}_{-0.12}$
QSAGE J023507.89+023507.9	38.78287	−4.03313	24.73 ± 0.19	0.3224	50	$7.27^{+0.29}_{-0.28}$	$10.1^{+0.3}_{-0.3}$	42^{+41}_{-40}	$-2.02^{+0.15}_{-0.23}$

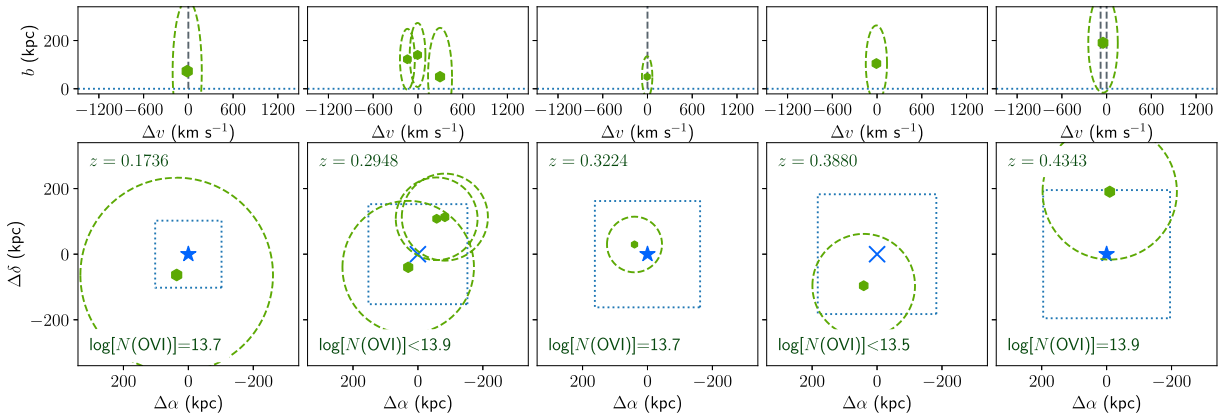

Figure 12. The velocity (top panels) and spatial (lower panels) distribution of galaxies (hexagons) around each of the $z < 0.68$ systems where one or more galaxies are found within $b = 2R_{\rm vir}$ of the sightline. The presence of any O VI absorption lines at each redshift is denoted by the vertical dashed lines in the top panels and a central blue star in the lower panels. Dashed circles centred on the galaxy positions illustrate the scales of $2R_{\rm vir}$ and $2\sigma_v$ for each galaxy. The dotted square in each spatial panel indicates the extent of the MUSE FOV at the system redshift.

$R_{\rm vir,12} \approx 195$ kpc for a $M_\star \approx 10^{12}$ $M_\odot$ mass galaxy), 154 kpc ($R_{\rm vir,12} \approx 176$ kpc), 156 kpc ($R_{\rm vir,12} \approx 174$ kpc), and 191 kpc ($R_{\rm vir,12} \approx 157$ kpc), respectively. Given previous studies at low redshift have found 'host' galaxies of O VI absorption at impact parameters of up to $b \approx 2R_{\rm vir}$, and some deep surveys at low redshift have found O VI absorbers at very large distances from the closest galaxy (Tripp et al. 2006; Johnson, Chen & Mulchaey 2013), it is not unreasonable that associated galaxies for these absorbers may fall outside of the field of view. Indeed, from a search of the NASA Extragalactic Database (NED) and the soon to be published CASBAH data, we find galaxies associated with these absorbers outside the MUSE field of view. In relation to the $z = 0.512$ absorber, we find a galaxy at $z = 0.511$ listed in NED, which is also detected in the WFC3 grism data via absorption features.

Taking the reverse, i.e. galaxies with no detectable associated O VI absorption in the sightline data, we find four such galaxies within $b \approx 2R_{\rm vir}$ of the sightline at $z < 0.68$. Three of these form a small grouping, lying within ≈600 km s^{-1} of each other at $z \approx 0.295$. The upper limit on any associated O VI coincident with this grouping is $N_{\rm O\,VI} < 10^{13.9}$ cm^{-2} (which we note is higher than the detected systems at $z < 0.68$).

3.1.2 Galaxy environments probed by the sightline at $z > 0.68$

Fig. 13 shows the galaxy distributions around each of the 5 O VI absorption systems detected at $z > 0.68$. In each case, galaxies within $\Delta v = \pm 680$ km s^{-1} are marked with green points, galaxies at -1600 km s^{-1} $< \Delta v < -680$ km s^{-1} with blue points, and galaxies at 680 km s^{-1} $< \Delta v <$ 1600 km s^{-1} with red points. Galaxies within this range that have been identified in the MUSE IFU data are given a black outline, whilst the estimated $2R_{\rm vir}$ scale for each galaxy is illustrated by the dashed ellipses. In each case $\Delta v = 0$ km s^{-1} is centred on the strongest component observed in the O VI absorption system at each redshift. The large dotted circle in each of the spatial panels shows the approximate field of view of the WFC3 observations at each redshift. As with the low redshift sample, we find the absorbers predominantly lie within ≈100 km s^{-1} of a nearby galaxy, except in the case of the absorber at $z \approx 0.73$. Additionally, the impact parameters in three of these cases are at scales of $b < 2R_{\rm vir}$.

The $z \approx 1.089$ strong ($N_{\rm OVI} = 10^{14.43 \pm 0.19}$ cm^{-2}) O VI absorber in the quasar spectrum coincides with a detected overdensity in the galaxy population. Four of the galaxies lie within $b = 200$ kpc of the quasar sightline, with three of these having velocities within a range of $\Delta v \approx 250$ km s^{-1} of each other (based on the MUSE [O II] measured redshifts). Of these three most closely associated galaxies, we find that the stellar mass is dominated by a $M_\star = 10^{10.0 \pm 0.1}$ $M_\odot$ galaxy, which lies at $\Delta v = +230$ km s^{-1} and $b = 170$ kpc from the absorption system. The remaining two closely associated galaxies are estimated to have masses of $M_\star \approx 10^{8.5}$ $M_\odot$.

Given the spatial and velocity distribution, we assume these to be the primary members forming a triplet/low-mass group (with the remaining galaxies at larger separations spatially and in velocity potentially tracing the large scale structure environment). Given only three detected members, it is not possible to reasonably estimate a halo mass from the velocity dispersion, however from the stellar mass, we infer a halo mass for the central group galaxy of $M_{\rm halo} = 10^{11.8 \pm 0.1}$ $M_\odot$. From this halo mass, we estimate a virial radius of $R_{\rm vir} \approx 90$ kpc, meaning the dominant galaxy lies at $b = 1.9R_{\rm vir}$ from the sightline.

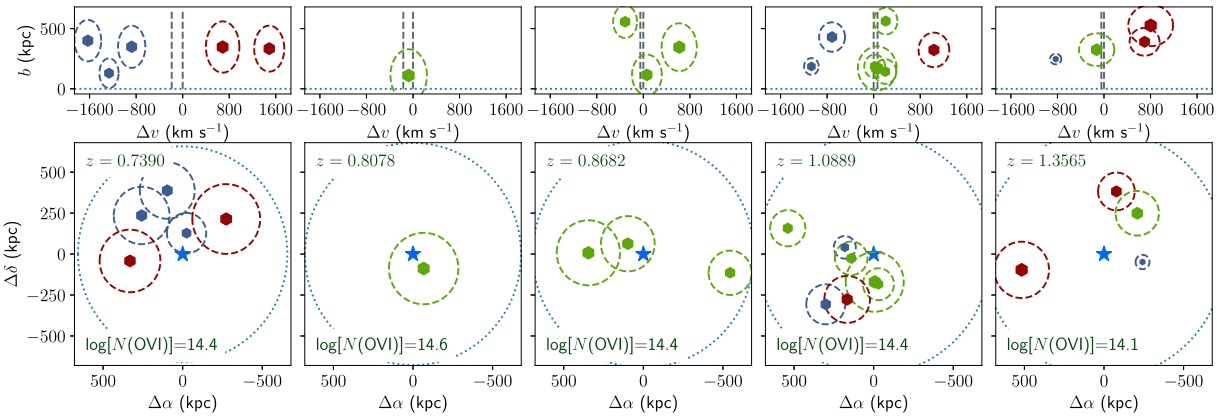

Figure 13. The velocity (top panels) and spatial (lower panels) distributions of galaxies at redshifts centred on detected O VI absorbers at $z > 0.68$. The sightline position is marked by a star in each case, whilst the O VI absorption lines at each redshift are denoted by the vertical dashed lines in the top panels. Galaxies marked in green are within $\Delta v < 680$ km s^{-1} of the absorber, whilst blue and red points denote galaxies blueshifted and redshifted by $\Delta v > 680$ km s^{-1} respectively. Points with a black hexagonal outline have been detected in [O II] emission in the MUSE datacube. We mark twice the inferred virial radii of each galaxy within $\Delta v = 1800$ km s^{-1} of the detected absorber. The large dotted circle marks the extent of the WFC3 grism data field of view at the redshift of interest.

For the $z \approx 0.73$ system, no galaxy lies within $\Delta_v < 680$ km s^{-1} of the absorber in the data sample. Indeed, this system may be a prospective candidate as the sightline tracing the cosmic web outside of galaxy haloes as discussed by Pessa et al. (2018). Those authors set a limit of $\frac{\Delta v}{\sigma_v}\frac{b}{R_{\rm vir}} > 2$ in their analysis to identify candidate cosmic web absorbers, which is clearly satisfied here (see Fig. 13 where the dashed ellipses in the top panels show the extent of $2\sigma_v$ in velocity space and $2R_{\rm vir}$ in impact parameter). We note that the redshift uncertainties on these galaxies (which lack MUSE coverage) are ≈680 km s^{-1} and as such the lack of alignment in velocity space could in part be due to the redshift accuracy of the galaxies.

Looking to the remaining overdense regions along the sightline as traced by the galaxy distribution. From the galaxy density, we find peaks above twice the median galaxy density at $z \approx 0.698$, $z \approx 0.977$, $z \approx 1.026$, $z \approx 1.089$, $z \approx 1.131$, and $z \approx 1.396$ (marked in Fig. 10). For each of these we plot the galaxy distribution, both spatially (lower panels) and in velocity space (top panels), around the sightline in Fig. 14 (except for the $z \approx 1.089$ system which has already been discussed and shown in Fig. 13). We centre the velocity axis in the top panels on the nearest galaxy (in units of $R_{\rm vir}$) to the sightline.

Overall, we find little sign of O VI absorption features tracing overdensities along the sightline probed, finding only one case out of 6 in which there is an association between detected O VI and a galaxy overdensity (i.e. the $z \approx 1.089$ system already discussed). Comparing to similar studies, Pointon et al. (2017) find 33 ± 16 per cent of their 18 galaxy groups align with detected O VI absorption. The Pointon et al. (2017) survey is at lower redshift and incorporates a greater number of galaxies at smaller impact parameters than our own sample, but despite this the two survey samples show approximately the same general trend for only a relatively small fraction of galaxy groups to align with strong O VI absorption.

3.2 The properties of O VI associated galaxies

Matter in the Universe is distributed hierarchically, such that galaxies exist within shared haloes. Assuming this present paradigm of hierarchically ordered dark matter haloes and sub-haloes, the conditions at any point within large scale structure can be driven and influenced by a number of components of the surrounding structure, e.g. the nearest galaxy, individual galaxies in the local neighbourhood, and as the overall mass and size scale of the matter halo hosting both the gas and the galaxies. As such (and combined with the large scales over which the O VI ion is observed around galaxies) it is worth identifying any correlations between not just the properties of the nearest galaxy to a given absorption system, but also to the wider galaxy population and environment. As discussed, this is one of the primary advantages of the strategy invoked in this survey, that we take a blind snapshot of the galaxy population around the quasar sightline.

We take two primary approaches in this section: (1) what are the observed properties of the most proximate galaxies to the sightline? and (2) what are those same properties for the most massive galaxies detected at each given redshift probed? The motivation for the latter is that, by isolating the most massive galaxies, these more closely relate the total structure mass that is being probed, thus opening the possibility of discerning any correlation between absorber properties and parent-halo properties (e.g. Oppenheimer et al. 2016; Nelson et al. 2018).

We begin by analysing the properties of galaxies lying closest in impact parameter to each O VI absorber, within our defined velocity window around an absorber redshift. These are shown in Fig. 15, with the absorber column density versus SFR of the nearest galaxy in the top panel and the absorber column density versus nearest galaxy stellar mass in the lower panel. In both cases, the red squares show the galaxy–absorber pairs at $z < 0.68$, whilst the $0.68 < z < 1.44$ pairs are split into two groups: those with $b < 2R_{\rm vir}$ (red hexagons); and those at $2R_{\rm vir} < b < 5R_{\rm vir}$ (grey triangles). In each case the paler points denote upper limits on O VI absorption, whilst the darker points denote significant detections. We show the $z < 0.2$ data-points of Werk et al. (2013) as the green diamonds in both panels.

At $z < 0.68$, we find three significant detections of O VI are coincident with galaxies. The galaxies cover a wide range of SFR (0.01 M$_\odot$ yr$^{-1} \lesssim$ SFR $\lesssim 2$ M$_\odot$ yr^{-1}) with stellar masses of $\log(M_\star/{\rm M}_\odot) \lesssim 10^{9.5}$, lower than those observed by Werk et al. (2013). We note that three of the associations are at $b/R_{\rm vir} \lesssim 1$ (i.e. equivalent to the Werk et al. 2013 sample), with the remaining two

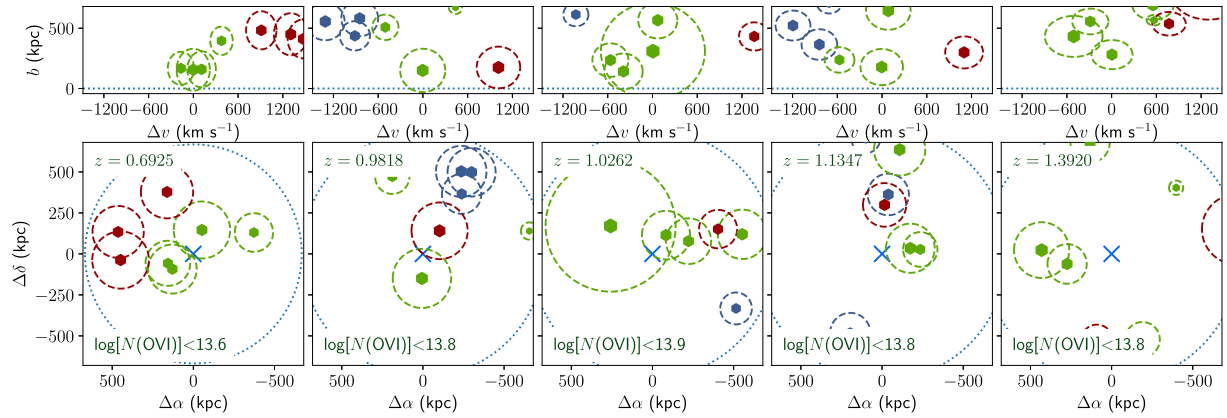

Figure 14. As in Fig. 13, but for the galaxy overdensity regions marked in Fig. 10. The sightline position is marked by a '×' symbol in each case.

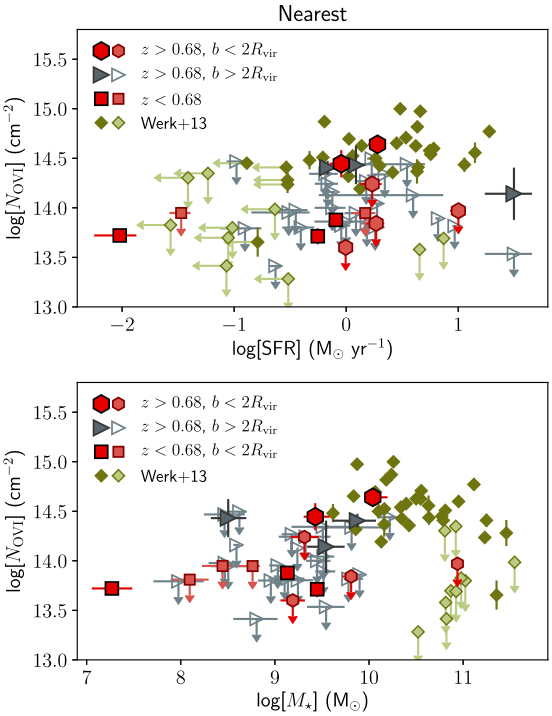

Figure 15. Sightline OVI absorber column density versus measured stellar mass (top panel) and SFR (lower panel) of the nearest galaxy within a velocity offset of $\Delta v_{\rm max}$ (as defined in the text). Red hexagons show O VI absorber–galaxy alignments at $0.68 < z < 1.44$ within $b = 2R_{\rm vir}$ of the sightline; grey triangles denote absorber–galaxy alignments at $0.68 < z < 1.44$ in the range $2R_{\rm vir} < b < 5R_{\rm vir}$ of the sightline; and blue squares denote $z < 0.68$ absorber–galaxy alignments. The paler points in each case highlight points where only upper limit measurements are available on the absorption. We show the $z < 0.2$ data points of Werk et al. (2013) as green diamonds in both panels for comparison.

at $1 \lesssim b/R_{\rm vir} \lesssim 2$. Our low redshift data are consistent with the spread of N(O VI) versus SFR data points in the Werk et al. (2013) results, although they show no correlation taken on their own.

At $z > 0.68$ and impact parameters of $b/R_{\rm vir} < 2$, our data show a large scatter in $N_{\rm O\,VI}$ for the star-forming galaxies, with several SFR $\approx$1 M$_\odot$ yr^{-1} galaxies coincident with O VI absorption of N(O VI) $\lesssim 10^{14}$ cm^{-2}. This particular field does not contain any $z \sim 1$ low-SFR galaxies, although we would have been able to identify such galaxies in the MUSE field of view, i.e. up to $\approx$300 kpc, to a magnitude limit of $i \approx 24$ if any were present. We note that the space density of passive galaxies to $i \lesssim 24$ at $z \sim 1$ is $n \approx 0.0003\,h^{-1}$ Mpc (e.g. Bielby et al. 2014), equating to $\approx$1 in a 1 arcmin^2, $0.68 < z < 1.44$ volume on average (i.e. not taking into account the highly clustered nature of such galaxies). Our data in this field can do little then to inform both the low-SFR range ($\lesssim 10^{-0.5}$ M$_\odot$ yr^{-1}) and by association the high-mass range beyond $M_\star \gtrsim 10^{11}$ M$_\odot$. However, the fact that we find such low limits on O VI absorption around star-forming galaxies has implications for any causal connection between ongoing star-formation in a galaxy and the detection of O VI ions in the galaxy's vicinity. Indeed, the large impact parameters involved, alongside recent kinematical studies (e.g. Nielsen et al. 2017), suggest that a causal connection between current SFR and O VI absorption systems is not universally applicable. Comparing to the low redshift Werk et al. (2013) data, we find a higher fraction of SFR $\approx$1 M$_\odot$ yr^{-1} galaxies with no detected coincident O VI absorption (at the N(O VI) $\lesssim 10^{14}$ cm^{-2} level) in our $z \sim 1$ data, although the larger impact parameters probed in our own sample compared to the Werk et al. (2013) data will inescapably be a significant contributing factor to this.

Moving to the O VI column density as a function of coincident galaxy stellar mass, the $z < 0.68$ sample shows all the absorber-galaxy pairs correspond to stellar masses of $M_\star \lesssim 10^{9.5}$ M$_\odot$ and column densities of N(O VI) $\lesssim 10^{14}$ cm^{-2}. Interestingly, combining this log($M_\star$/M$_\odot$) $\approx 10^{9.5}$ sample with the Werk et al. (2013) data (with the caveat that two of our data points are at larger impact parameters than present in the Werk et al. 2013 data), shows some suggestion of a transition from low to high column densities around a proximate galaxy stellar mass of $M_\star \sim 10^{9.5}$ M$_\odot$. The higher redshift sample primarily probes stellar masses of $\approx 10^{9-10}$ M$_\odot$, i.e. coincident with the possible transition region in the low redshift data. Indeed, the $z \sim 1$ data tentatively support this picture of an increase in O VI column density at stellar masses in the range $\approx 10^{9.5-10}$ M$_\odot$. In addition, we find a single galaxy-absorber pair corresponding to a galaxy with stellar mass $M_\star \approx 10^{11}$ M$_\odot$. This higher mass point corresponds to an O VI upper limit of N(O VI) $\lesssim 10^{11}$ cm^{-2} and overlaps with the regime in the low-redshift data of Werk et al. (2013) where a large fraction of galaxies show no detectable sightline O VI absorption. The small number of data points in this first analysis is restrictive in making any strong conclusions however.

We now reproduce the plot of column density versus galaxy properties from Fig. 15, but with the SFR (top panel) and stellar mass

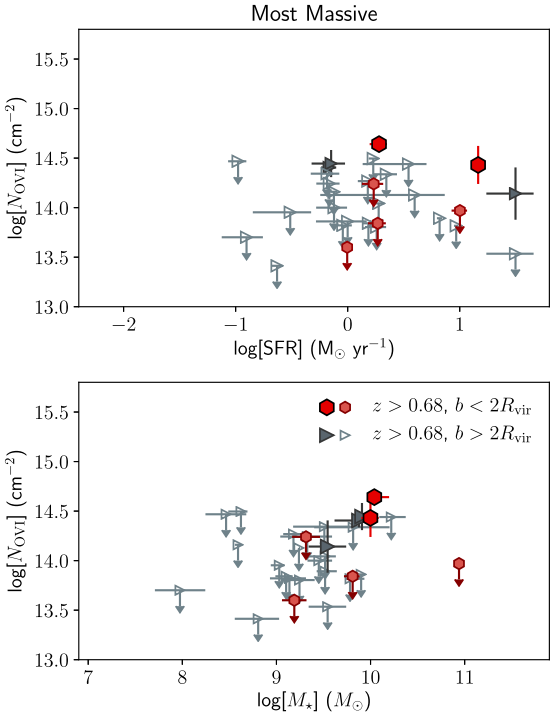

Figure 16. As in Fig. 15 but taking the stellar mass and SFR properties for the most massive proximate galaxies (i.e. up to $5R_{vir}$). Only the $0.68 < z < 1.44$ sample is now shown, given the more limited field of view of the $z < 0.68$ data.

(lower panel) of the most massive galaxies lying at the redshift of each absorption system in Fig. 16. The symbols used are consistent with those in Fig. 15. For clarity and given the smaller field of view probed by MUSE, we omit the $z < 0.68$ O VI absorber–galaxy pairs.

This change of 'host galaxy' selection affects two absorber–galaxy pairs: one at $b/R_{vir} < 2$ and one at $b/R_{vir} \approx 3$ (≈350 kpc). The N(O VI) versus SFR distribution shows no indication of any correlations given the available data. The distribution of points shows a large scatter in column densities across the full SFR range probed. For the stellar mass, in the case of both shifted data points, the most massive galaxy detected at the absorber redshifts have estimated stellar masses of $\approx 10^{10}$ M$_\odot$. For the $z \sim 1$ galaxies with stellar masses of $\lesssim 10^{9.5}$ M$_\odot$, we effectively detect no O VI absorption unless a more massive galaxy (i.e. $\gtrsim 10^{9.5}$ M$_\odot$) is also present. At $M_\star > 10^{10}$ M$_\odot$, our dataset from this first field poorly samples the galaxy population, with only a single massive galaxy in this range (which corresponds to an O VI limit of $N_{O\,VI} \approx 10^{13.9}$ cm^{-2}).

In summary, we find a marginal preference for the N(O VI) $\approx 10^{14.5}$ cm^{-2} absorbers to be associated with galaxies of stellar masses $M_\star \approx 10^{10}$ M$_\odot$ (for both galaxy–absorber pairs lying at $b < 2R_{vir}$ and $b < 5R_{vir}$). The detections of O VI absorption in the sightline all lie at the redshift of a galaxy within a mass range of $10^{9.5}$ M$_\odot$ $< M_\star < 10^{10}$ M$_\odot$, whilst the non-detections that also lie in this mass range offer only relatively poorly constrained upper limits of $N_{O\,VI} \approx 10^{14.3}$ cm^{-2}.

3.3 Covering fraction of O VI around $z \approx 1$ galaxies

We now calculate the covering fraction of O VI around the galaxy population as a function of impact parameter, galaxy stellar mass and galaxy star-formation rate. For this, we include all galaxies around the sightline and not just the nearest or most massive. We measure the covering fraction for O VI column densities of $N_{O\,VI} > 10^{14}$ cm^{-2}, such that the covering fraction is given by $c = \frac{n_{gal(N>10^{14})}}{n_{gal}}$. Galaxies found within $\Delta_v = \max\{\sigma_v, 400$ km s$^{-1}\}$ of a column density upper limit of $N_{O\,VI} > 10^{14}$ cm^{-2} (with no corresponding significant detection) are not included in the calculation (i.e. as these are likely the result of contamination from other absorption lines masked in the analysis).

The resulting covering fraction of O VI absorbers with column densities of $N > 10^{14}$ cm^{-2} is shown as a function of impact parameter (in units of the virial radius) in the left-hand panel of Fig. 17. We find a trend for increasing covering fraction with decreasing impact parameter in the $0.68 < z < 1.5$ sample, with covering fractions of $c \approx 0.2$ up to $b/R_{vir} = 4$. Covering fractions based on Werk et al. (2013) and Kacprzak et al. (2015) are shown by the green diamonds and blue plus symbols respectively. As described previously, the Werk et al. (2013) data are primarily higher mass and lower redshift than our own data, whilst the Kacprzak et al. (2015) data lie at $z \lesssim 0.5$ and are comparable in stellar mass range to our own data. Clearly our own sample predominantly probes large scales in impact parameter than these previous works. Agreement is seen where the QSAGE data overlap with the Kacprzak et al. (2015) data at $1 < b/R_{vir} < 2$.

In the central panel of Fig. 17, we show the covering fraction for galaxies split into two mass bins: $M_\star < 10^{9.6}$ M$_\odot$ and $10^{9.6}$ M$_\odot$ $< M_\star < 10^{10.6}$ M$_\odot$. We find a moderately significant relation between covering fraction and stellar mass at $b/R_{vir} \approx 2$, with the higher mass galaxies showing a higher covering fraction. Again, we show covering fractions based on the data of Werk et al. (2013), now split in bins of $10^{9.6}$ M$_\odot$ $< M_\star < 10^{10.6}$ M$_\odot$ (i.e. matching our own higher mass sample) and $M_\star > 10^{10.6}$ M$_\odot$ (i.e. masses higher than probed by our own data). This shows an inversion with respect to our own results, where the higher mass sample now has a lower covering fraction (albeit at only the 1σ level).

The right-hand panel shows the covering fraction split into samples based on an SFR limit of $10^{0.25}$ M$_\odot$ yr^{-1}. In this case we find no sign of a difference of the covering fraction based on the two different samples, in contrast to the low-redshift/low impact parameter covering fractions from the COS-Haloes sample (Werk et al. 2013, green diamonds), where a significant dependence on SFR is seen.

4 DISCUSSION

Our results have shown tentative evidence for O VI absorption preferentially being found in the vicinity of moderate mass ($M_\star \approx 10^{9.5–10}$ M$_\odot$) star-forming galaxies. The star-forming properties of these $z \approx 1$ galaxies are comparable (SFR $\gtrsim 1$ M$_\odot$ yr^{-1}) to that observed for isolated $L^\star$ galaxies at low redshift coincident with O VI absorption (Tumlinson et al. 2011; Werk et al. 2014; Kacprzak et al. 2015).

We have reported on O VI absorption systems found up to scales of ≈300–400 kpc ($\approx 4R_{vir}$) from the nearest galaxy, comparable to the largest field of view low redshift surveys of such absorbers (e.g. Mathes et al. 2014; Johnson et al. 2015a; Pointon et al. 2017)

Prochaska et al. (2011) at low redshift similarly find a picture whereby the association between galaxies and O VI shows a strong dependence on galaxy luminosity. They find O VI absorption most commonly to be found within $b \approx 200–300$ kpc of a $0.1L^\star < L < 1L^\star$ (intermediate sub-$L^\star$) galaxies, and that where a dwarf galaxy is found closest to O VI sightline absorption, there often also exists

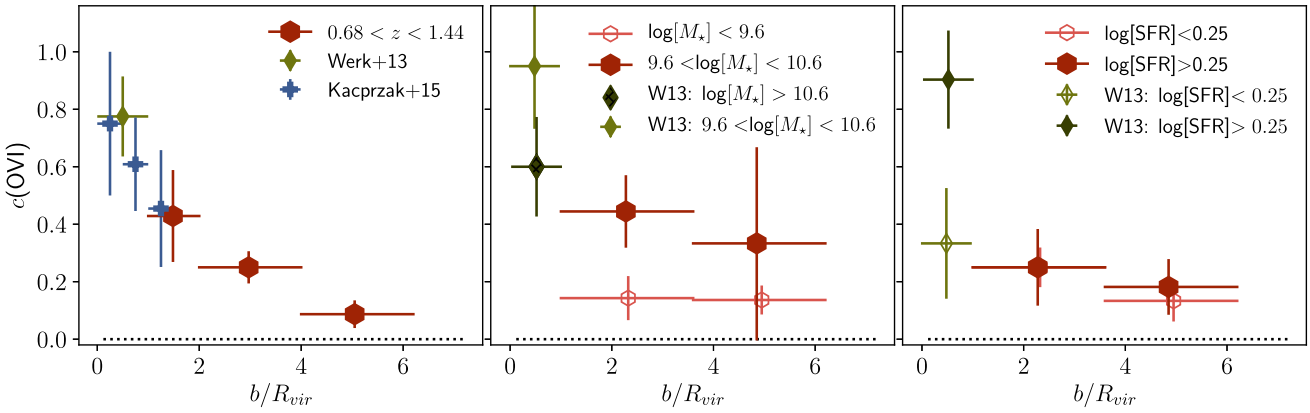

Figure 17. The covering fraction of $N_{\rm O\,VI} > 10^{14}$ cm^{-2} O VI absorbers as a function of impact parameter (left-hand panel); separated into mass bins at $M_\star = 10^{9.6}$ M$_\odot$ (centre panel); and separated into SFR bins at SFR $= 10^{0.25}$ M$_\odot$ yr^{-1} (right-hand panel). The green diamonds shown in all three panels show covering fractions based on Werk et al. (2013), whilst the plus symbols in the left-hand panel show covering fractions from Kacprzak et al. (2015).

an intermediate sub-$L^\star$ galaxy within $b \approx 300$ kpc of that same absorber. However, it is clear from low redshift studies that O VI systems arise from a diverse array of galaxy environments ranging from dwarfs to sub-L∗–L∗ galaxies and even more massive systems. Prochaska et al. (2011) show that some dwarf galaxies without more massive neighbours are associated with O VI absorption systems. Indeed, Johnson et al. (2013) showed that a fraction of O VI absorbers arise in low-mass galaxy groups with star-forming members that are all <0.1 L∗. Moreover, Johnson et al. (2017) showed that star-forming field dwarfs of <0.1 L∗ without massive neighbours account for ≈20 per cent of O VI absorption systems with rest equivalent widths stronger than ≈0.1Å, and that this phase of their CGM likely dominates the baryon budget of these low-mass systems. More recently, Chen et al. (2018) and Zahedy et al. (2019) showed that O VI absorption systems with log$N$(O VI) > 13.5 are common in the CGM of luminous, quiescent galaxies.

Two of the $z > 0.68$ absorption systems are coincident with multiple galaxies in our survey (a galaxy pair at $z \approx 0.868$ and the galaxy triplet group at $z \approx 1.089$), whilst around 3 we detect only a single galaxy given our survey limits. We find a more massive ($M_{\rm halo} \approx 10^{12.6}$ M$_\odot$) group system for which we detect no O VI absorption at $z = 1.026$. In this first QSAGE field, given the relatively small volume covered, we have only a single galaxy with which to probe the higher mass galaxy environment beyond $M_\star \gtrsim 10^{10.5}$ M$_\star$. At $M_\star \approx 10^{10.9}$ M$_\star$, this galaxy and its associated group shows no detectable O VI in the sightline data.

Incorporating low redshift results, Tumlinson et al. (2011) find 50 per cent of galaxies at $M_\star \gtrsim 10^{10.5}$ M$_\odot$ show associated O VI absorption, compared to 100 per cent at $10^{9.5}$ M$_\odot \lesssim M_\star \lesssim 10^{10.5}$ M$_\odot$. At the upper end of the latter range, Muzahid et al. (2015) report on an extremely strong O VI absorption system associated with a $M_{\rm halo} \approx 10^{12.5}$ M$_\odot$ star-forming galaxy. Stocke et al. (2014) report the alignment of warm O VI absorbers with several galaxy groups at $z \lesssim 0.2$, with group velocity dispersions of $\sigma_v \approx 100$–600 km s^{-1}. This equates approximately to a halo mass range of $M_{\rm halo} \approx 10^{12.5\text{–}14.5}$ M$_\odot$, suggesting groups of all masses, up to low-mass clusters have the potential to exhibit warm gas capable of being detected in O VI absorption. Pointon et al. (2017) find approximately a third of low-mass galaxy groups (≈2–5 members) in their sample exhibit O VI absorption, whilst Burchett et al. (2018) found no O VI absorption within cluster haloes at $M_{\rm halo} \approx 10^{14\text{–}14.5}$ M$_\odot$. The caveat remains, however, that it is not often clear whether the halo gas probed by a given sightline is reflecting the nature of the properties

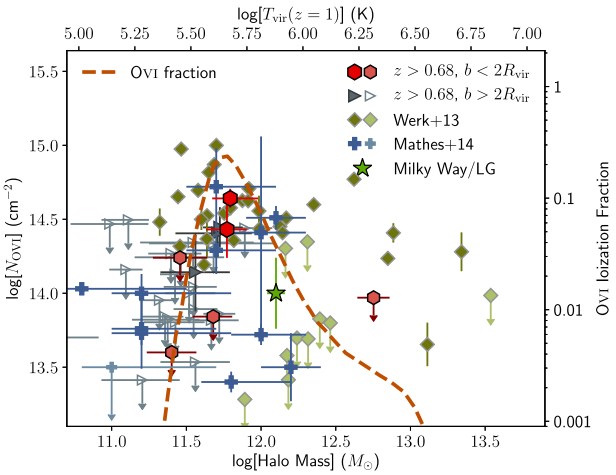

Figure 18. Column densities of O VI absorbers versus their estimated dark matter halo mass for the $z > 0.68$ galaxy sample based on identified associations from Fig. 16. Hexagons denote associated galaxies within $b = 2R_{\rm vir}$, whilst triangles denote associated galaxy–absorber pairs at impact parameters of $2R_{\rm vir} < b < 5R_{\rm vir}$. The dashed curve shows the predicted O VI ionization fraction for a given halo mass, assuming the halo gas being probed to be close to the virial temperature of the halo. Green diamonds and blue plus symbols show the results of Werk et al. (2013) and Mathes et al. (2014), respectively.

of a sub-halo or the overall group halo (e.g. Stocke et al. 2017), whilst star-forming winds remain a potentially significant influence on the presence of warm gas at small scales (e.g. Tripp et al. 2011; Tumlinson et al. 2011)

If some fraction of O VI absorbing gas is simply diffuse halo gas, collisionally ionized at approximately the virial temperature of the host dark matter halo, then we may expect to see some sort of peak in the column density distribution at some halo mass. Indeed, this is predicted by simulations such as shown by Mulchaey et al. (1996), Oppenheimer et al. (2016) and Nelson et al. (2018). Following this reasoning, we show in Fig. 18 the inferred halo masses for the $z > 0.68$ sample assuming the absorbers to be associated with the most massive proximate galaxy (i.e. within $b = 2R_{\rm vir}$; dark red hexagons). We find that the $N_{\rm O\,VI} \gtrsim 10^{14}$ cm^{-2} O VI absorption is generally found within the proximity of a galaxy corresponding to a $10^{11.5}$ M$_\odot \lesssim M_{\rm halo} \lesssim 10^{12}$ M$_\odot$ halo mass. Upper limits on the

O VI column density adjacent to other galaxies along the sightline (within $0.68 < z < 1.4$) preferentially show upper-limit constraints indicating lower levels of the O VI ion.

The dashed curve shows the predicted O VI ionization fraction assuming that the halo gas being probed is at temperatures of ≈70 per cent of the virial temperature (i.e. accounting for predicted halo temperature profiles e.g. Komatsu & Seljak 2001). This provides a simple physical picture in which the detected gas represents a diffuse warm halo component (e.g. Mathews & Prochaska 2017). For comparison to our own data, we also show the low-redshift results of Werk et al. (2013, green diamonds) and Mathes et al. (2014, blue plus symbols). The Werk et al. (2013) sample is dominated by strong O VI detections at $10^{11.5}\,M_{\odot} \lesssim M_{\rm halo} \lesssim 10^{12}\,M_{\odot}$, whilst the scatter increases at $M_{\rm halo} \gtrsim 10^{12}\,M_{\odot}$. Similarly, the strong absorbers (N(O VI) ≈ $10^{14.5}$ cm^{-2}) detected in the Mathes et al. (2014) sample are coincident with galaxies with estimated halo masses of $M_{\rm halo} \lesssim 10^{12}\,M_{\odot}$. Similar to our own data and that of Werk et al. (2013), there is also a lot of scatter with a number of low-column density systems (or upper limits) coincident with comparable galaxy halo masses. The evidence is not clear-cut then, although the scatter may be the effect of a patchy/clumpy halo medium (Lopez et al. 2018), or AGN heating of the gas (Oppenheimer et al. 2018b).

The EAGLE hydrodynamical simulations (Crain et al. 2015; Schaye et al. 2015) predict that the O VI column density peaks ($N_{\rm O\,VI} \approx 10^{14.2}$ cm^{-2}) for galaxies in haloes of masses $\approx 10^{11.7-12.4}\,M_{\odot}$, with the gas within lower mass haloes too cool, and the gas within higher mass haloes too hot, to lead to significant O VI absorption in quasar sightlines (albeit at $z = 0.2$; Oppenheimer et al. 2016). Similarly, the IllustrisTNG predicts, at $z = 0$, that O VI should be predominantly found in diffuse $T \approx 10^{5.6\pm0.2}$ K haloes of half-mass radii $\approx 10^{2.1\pm0.2}$ kpc around $M_{\star} \approx 10^{10.2\pm0.3}\,M_{\odot}$ galaxies (Nelson et al. 2018). Alternatively, the O VI gas may trace low-pressure gas photoionized by the UV background (e.g. Stern et al. 2016, 2018). In this case clouds are hierarchically embedded in the CGM structure, allowing for a patchy medium and potentially explaining the large scatter in column densities that we measure.

Finally, we note that the halo masses that we find associated with the O VI absorbers are comparable to the mass of the Local Group. Indeed, observations of the Milky Way's halo have shown detection of O VI absorption ($N_{\rm O\,VI} \gtrsim 10^{13.6}$ cm^{-2}) in ≈70 per cent of sightlines through the halo (e.g. Sembach et al. 2003; Wakker et al. 2003). The halo mass of the Milky Way is estimated to be $M_{\rm halo} \approx 10^{12}\,M_{\odot}$ (e.g. Callingham et al. 2019), whilst the mass of the Local Group as a whole is estimated to be $M_{\rm halo} \approx 2 \times 10^{12}\,M_{\odot}$ (e.g. Courteau & van den Bergh 1999).

5 CONCLUSIONS

We have presented methods and results from the first field in the QSAGE survey – a blind *HST*/WFC3 grism survey of galaxies in the region of bright $z > 1.2$ quasars with archival *HST*/STIS and COS spectra. Our key results are as follows:

(i) We find O VI up to impact parameters of $b \approx 350$ kpc from the nearest detected galaxy at $0.68 < z < 1.42$. Column densities of absorbers over the impact parameters probed ($100 < b < 400$ kpc) show a large scatter, corresponding to covering fractions of c(O VI) $\lesssim 0.5$ (for N(O VI) $> 10^{14}$ cm^{-2}).

(ii) Whilst all five of the detected $z \approx 1$ O VI absorbers are found to lie within $b \approx 400$ kpc of a star-forming galaxy, we also find comparably star-forming galaxies within the same range in impact parameter with no detected O VI absorption. Taking a limit in impact parameter of $b = 2R_{\rm vir}$, we find 50 per cent of the sample relate to upper limits on the sightline O VI column density of $N_{\rm O\,VI} \lesssim 10^{13.9}$ cm^{-2}.

(iii) We identify a low-mass galaxy group at $z = 1.08$ coincident in redshift with significant O VI absorption in the quasar sightline, potentially probing the intra-group medium. The group consists of three confirmed members and estimate a group halo mass of $M_{\rm halo} \approx 10^{11.8}\,M_{\odot}$. We find several further galaxy overdensities close to the sightline, with estimated halo masses of up to $M_{\rm halo} \approx 10^{12.8}\,M_{\odot}$. None are coincident with detected O VI absorption to a detection limit of $N_{\rm O\,VI} \lesssim 13.9$ cm^{-2}.

(iv) Estimating the host halo masses of $N_{\rm O\,VI} \gtrsim 10^{14}$ cm^{-2} absorbers suggests the majority of such absorbers are found in the proximity of haloes of mass $M_{\rm halo} \approx 10^{11.8}\,M_{\odot}$, consistent with diffuse gas at the virial temperature of such haloes. Significantly, we find a higher covering fraction of $N_{\rm O\,VI} \geq 10^{14}$ cm^{-2} absorbers around higher mass star-forming galaxies (at $\approx 2\sigma$) at impact parameters of $\lesssim 4R_{\rm vir}$.

This first of 12 fields from our *HST* WFC3 Large Programme, QSAGE, acts as a proof of concept of what the full survey can deliver. Whilst we have focused on tracing the properties of the galaxy population around O VI absorbers here, these data will provide a comprehensive basis for studies of the CGM across a range of absorption species, allowing insights into a broad range of phases of material within the CGM.

ACKNOWLEDGEMENTS

We first thank S. Johnson, G. Kacprzak, and the anonymous referee for their input on this work. RMB, MF, RGB, and SLM acknowledge the Science and Technology Facilities Council (STFC) through grants ST/P000541/1 and ST/L00075X/1 for support. This project has received funding from the European Research Council (ERC) under the European Union's Horizon 2020 research and innovation programme (grant agreement no. 757535). TMT, JNB, and JXP received financial support for this research through NASA Grant *HST*-GO-11741 from the Space Telescope Science Institute, which is operated by the Association of Universities for Research in Astronomy, Inc., under NASA Contract NAS5-26555. This work is based in part on observations obtained with MegaPrime/MegaCam, a joint project of CFHT and CEA/IRFU (Commisariat à l'énergie et atomique et aux énergies alternative/Institut de recherche de lois fondamentales de l'Univers), at the Canada–France–Hawaii Telescope (CFHT) which is operated by the National Research Council (NRC) of Canada, the Centre National de la Recherche Scientifique (CNRS) of France, and the University of Hawaii. The data used in this paper are available via the Mikulski Archive for Space Telescopes (*HST* COS, STIS, and WFC3 data), the Canadian Astronomy Data Centre (CFHTLS data), and the ESO archive (VLT/MUSE data). The WHT/ACAM imaging data are available at http://astro.dur.ac.uk/qsage/. We have produced data products using LE PHARE and GAZPAR (located at the Laboratoire d'Astrophysique de Marseille) and we thank O. Ilbert for support in using these. This research made use of ASTROPY, a community-developed core PYTHON package for Astronomy (Astropy Collaboration 2018). In the course of this work, we made use of A. Rohatgi's WEBPLOTDIGITIZER (http://arohatgi.info/WebPlotDigitizer/).

REFERENCES

Adelberger K. L., Shapley A. E., Steidel C. C., Pettini M., Erb D. K., Reddy N. A., 2005, ApJ, 629, 636
Adelberger K. L., Steidel C. C., Shapley A. E., Pettini M., 2003, ApJ, 584, 45
Aracil B., Tripp T. M., Bowen D. V., Prochaska J. X., Chen H.-W., Frye B. L., 2006, MNRAS, 367, 139
Arnouts S., Cristiani S., Moscardini L., Matarrese S., Lucchin F., Fontana A., Giallongo E., 1999, MNRAS, 310, 540
Astropy Collaboration, 2018, AJ, 156, 123
Bacon R. et al., 2010, in McLean I. S., Ramsay S. K., Takami H., eds, Proc. SPIE Conf. Ser. Vol. 7735, Ground-based and Airborne Instrumentation for Astronomy III. SPIE, Bellingham, p. 773508
Behroozi P. S., Wechsler R. H., Conroy C., 2013, ApJ, 770, 57
Bergeron J., Boissé P., 1991, A&A, 243, 344
Bertin E., 2006, in Gabriel C., Arviset C., Ponz D., Enrique S., eds, ASP Conf. Ser. Vol. 351, Astronomical Data Analysis Software and Systems XV. Astron. Soc. Pac., San Francisco, p. 112
Bertin E., Arnouts S., 1996, A&AS, 117, 393
Bertin E., Mellier Y., Radovich M., Missonnier G., Didelon P., Morin B., 2002, in Bohlender D. A., Durand D., Handley T. H., eds, ASP Conf. Ser. Vol. 281, Astronomical Data Analysis Software and Systems XI. Astron. Soc. Pac., San Francisco, p. 228
Bielby R., Crighton N. H. M., Fumagalli M., Morris S. L., Stott J. P., Tejos N., Cantalupo S., 2017a, MNRAS, 468, 1373
Bielby R. M. et al., 2014, A&A, 568, A24
Bielby R. M. et al., 2017b, MNRAS, 471, 2174
Bouché N., Hohensee W., Vargas R., Kacprzak G. G., Martin C. L., Cooke J., Churchill C. W., 2012, MNRAS, 426, 801
Bouché N. et al., 2010, ApJ, 718, 1001
Bowen D. V. et al., 2006, ApJ, 645, L105
Brammer G., Ryan R., Pirzkal N., 2015, Technical Report, Source-dependent Master Sky Images for the WFC3/IR Grisms
Brammer G. B. et al., 2012, ApJS, 200, 13
Bruzual G., Charlot S., 2003, MNRAS, 344, 1000
Bryan G. L., Norman M. L., 1998, ApJ, 495, 80
Burchett J. N., Tripp T. M., Wang Q. D., Willmer C. N. A., Bowen D. V., Jenkins E. B., 2018, MNRAS, 475, 2067
Burchett J. N. et al., 2015, ApJ, 815, 91
Burchett J. N. et al., 2016, ApJ, 832, 124
Callingham T. M. et al., 2019, MNRAS, 484, 5453
Calzetti D., Armus L., Bohlin R. C., Kinney A. L., Koornneef J., Storchi-Bergmann T., 2000, ApJ, 533, 682
Cardelli J. A., Clayton G. C., Mathis J. S., 1989, ApJ, 345, 245
Chabrier G., 2003, PASP, 115, 763
Chen H.-W., Helsby J. E., Gauthier J.-R., Shectman S. A., Thompson I. B., Tinker J. L., 2010, ApJ, 714, 1521
Chen H.-W., Lanzetta K. M., Webb J. K., Barcons X., 1998, ApJ, 498, 77
Chen H.-W., Lanzetta K. M., Webb J. K., Barcons X., 2001, ApJ, 559, 654
Chen H.-W., Mulchaey J. S., 2009, ApJ, 701, 1219
Chen H.-W., Zahedy F. S., Johnson S. D., Pierce R. M., Huang Y.-H., Weiner B. J., Gauthier J.-R., 2018, MNRAS, 479, 2547
Cochrane R. K., Best P. N., Sobral D., Smail I., Geach J. E., Stott J. P., Wake D. A., 2018, MNRAS, 475, 3730
Correa C. A., Schaye J., Wyithe J. S. B., Duffy A. R., Theuns T., Crain R. A., Bower R. G., 2018, MNRAS, 473, 538
Coupon J. et al., 2012, A&A, 542, A5
Courteau S., van den Bergh S., 1999, AJ, 118, 337
Crain R. A. et al., 2015, MNRAS, 450, 1937
Crighton N. H. M., Morris S. L., Bechtold J., Crain R. A., Jannuzi B. T., Shone A., Theuns T., 2010, MNRAS, 402, 1273
Crighton N. H. M. et al., 2011, MNRAS, 414, 28
Cuillandre J.-C. J. et al., 2012, in Peck A. B., Seaman R. L., Comeron F., eds, Proc. SPIE Conf. Ser. Vol. 8448, Observatory Operations: Strategies, Processes, and Systems IV. SPIE, Bellingham, p. 84480M
Davé R., Finlator K., Oppenheimer B. D., 2012, MNRAS, 421, 98
Dekel A. et al., 2009, Nature, 457, 451
Faisst A. L., Masters D., Wang Y., Merson A., Capak P., Malhotra S., Rhoads J. E., 2018, ApJ, 855, 132
Farina E. P., Falomo R., Scarpa R., Decarli R., Treves A., Kotilainen J. K., 2014, MNRAS, 441, 886
Finn C. W. et al., 2016, MNRAS, 460, 590
Fumagalli M., Cantalupo S., Dekel A., Morris S. L., O'Meara J. M., Prochaska J. X., Theuns T., 2016, MNRAS, 462, 1978
Fumagalli M., Fossati M., Hau G. K. T., Gavazzi G., Bower R., Sun M., Boselli A., 2014, MNRAS, 445, 4335
Fumagalli M., Haardt F., Theuns T., Morris S. L., Cantalupo S., Madau P., Fossati M., 2017a, MNRAS, 467, 4802
Fumagalli M., Prochaska J. X., Kasen D., Dekel A., Ceverino D., Primack J. R., 2011, MNRAS, 418, 1796
Fumagalli M. et al., 2017b, MNRAS, 471, 3686
Fynbo J. P. U. et al., 2018, MNRAS, 479, 2126
Garn T., Best P. N., 2010, MNRAS, 409, 421
Gilbank D. G., Baldry I. K., Balogh M. L., Glazebrook K., Bower R. G., 2010, MNRAS, 405, 2594
Green J. C. et al., 2012, ApJ, 744, 60
Haro G., Luyten W. J., 1962, Bol. Obs. Tonantzintla Tacubaya, 3, 37
Hinton S. R., Davis T. M., Lidman C., Glazebrook K., Lewis G. F., 2016, Astron. Comput., 15, 61
Hummels C. B., Bryan G. L., Smith B. D., Turk M. J., 2013, MNRAS, 430, 1548
Ilbert O. et al., 2006, A&A, 457, 841
Ilbert O. et al., 2010, ApJ, 709, 644
Jannuzi B. T. et al., 1998, ApJS, 118, 1
Johnson H. L. et al., 2018, MNRAS, 474, 5076
Johnson S. D., Chen H.-W., Mulchaey J. S., 2013, MNRAS, 434, 1765
Johnson S. D., Chen H.-W., Mulchaey J. S., 2015a, MNRAS, 449, 3263
Johnson S. D., Chen H.-W., Mulchaey J. S., 2015b, MNRAS, 452, 2553
Johnson S. D., Chen H.-W., Mulchaey J. S., Schaye J., Straka L. A., 2017, ApJ, 850, L10
Kacprzak G. G., Churchill C. W., Nielsen N. M., 2012, ApJ, 760, L7
Kacprzak G. G., Muzahid S., Churchill C. W., Nielsen N. M., Charlton J. C., 2015, ApJ, 815, 22
Kacprzak G. G. et al., 2019, ApJ, 870, 137
Karim A. et al., 2011, ApJ, 730, 61
Kennicutt R. C., Jr., 1998, ARA&A, 36, 189
Kewley L. J., Geller M. J., Jansen R. A., 2004, AJ, 127, 2002
Kimble R. A. et al., 1998, ApJ, 492, L83
Komatsu E., Seljak U., 2001, MNRAS, 327, 1353
Kümmel M., Walsh J. R., Pirzkal N., Kuntschner H., Pasquali A., 2009, PASP, 121, 59
Lagos C. D. P., Lacey C. G., Baugh C. M., Bower R. G., Benson A. J., 2011, MNRAS, 416, 1566
Lilly S. J., Le Fevre O., Hammer F., Crampton D., 1996, ApJ, 460, L1
Lopez S. et al., 2018, Nature, 554, 493
Lovegrove E., Simcoe R. A., 2011, ApJ, 740, 30
Madau P., Ferguson H. C., Dickinson M. E., Giavalisco M., Steidel C. C., Fruchter A., 1996, MNRAS, 283, 1388
Mathes N. L., Churchill C. W., Kacprzak G. G., Nielsen N. M., Trujillo-Gomez S., Charlton J., Muzahid S., 2014, ApJ, 792, 128
Mathews W. G., Prochaska J. X., 2017, ApJ, 846, L24
Meiring J. D., Tripp T. M., Werk J. K., Howk J. C., Jenkins E. B., Prochaska J. X., Lehner N., Sembach K. R., 2013, ApJ, 767, 49
Meiring J. D. et al., 2011, ApJ, 732, 35
Momcheva I. G. et al., 2016, ApJS, 225, 27
Morris S. L., Jannuzi B. T., 2006, MNRAS, 367, 1261
Morris S. L., Weymann R. J., Dressler A., McCarthy P. J., Smith B. A., Terrile R. J., Giovanelli R., Irwin M., 1993, ApJ, 419, 524
Morris S. L., Weymann R. J., Savage B. D., Gilliland R. L., 1991, ApJ, 377, L21
Mulchaey J. S., Mushotzky R. F., Burstein D., Davis D. S., 1996, ApJ, 456, L5
Muzahid S., Kacprzak G. G., Churchill C. W., Charlton J. C., Nielsen N. M., Mathes N. L., Trujillo-Gomez S., 2015, ApJ, 811, 132
Nelson D. et al., 2018, MNRAS, 477, 450

Nielsen N. M., Churchill C. W., Kacprzak G. G., 2013, ApJ, 776, 115
Nielsen N. M., Kacprzak G. G., Muzahid S., Churchill C. W., Murphy M. T., Charlton J. C., 2017, ApJ, 834, 148
Oppenheimer B. D., Schaye J., Crain R. A., Werk J. K., Richings A. J., 2018b, MNRAS, 481, 835
Oppenheimer B. D., Segers M., Schaye J., Richings A. J., Crain R. A., 2018a, MNRAS, 474, 4740
Oppenheimer B. D. et al., 2016, MNRAS, 460, 2157
Osterman S. et al., 2011, Ap&SS, 335, 257
Penton S. V., Stocke J. T., Shull J. M., 2002, ApJ, 565, 720
Pessa I. et al., 2018, MNRAS, 477, 2991
Planck Collaboration XIII, 2016, A&A, 594, A13
Pointon S. K., Nielsen N. M., Kacprzak G. G., Muzahid S., Churchill C. W., Charlton J. C., 2017, ApJ, 844, 23
Prochaska J. X., Lau M. W., Hennawi J. F., 2014, ApJ, 796, 140
Prochaska J. X., Weiner B., Chen H.-W., Mulchaey J., Cooksey K., 2011, ApJ, 740, 91
Prochaska J. X. et al., 2013, ApJ, 776, 136
Prochaska J. X. et al., 2017, ApJ, 837, 169
Péroux C. et al., 2017, MNRAS, 464, 2053
Rahmati A., Pawlik A. H., Raičević M., Schaye J., 2013, MNRAS, 430, 2427
Rahmati A., Schaye J., Bower R. G., Crain R. A., Furlong M., Schaller M., Theuns T., 2015, MNRAS, 452, 2034
Rakic O., Schaye J., Steidel C. C., Rudie G. C., 2012, ApJ, 751, 94
Riley A. et al., 2018, STIS Instrument Hanbook, Version 17.0, STScI, Baltimore
Rubin K. H. R., Weiner B. J., Koo D. C., Martin C. L., Prochaska J. X., Coil A. L., Newman J. A., 2010, ApJ, 719, 1503
Savage B. D. et al., 2010, ApJ, 719, 1526
Schaye J. et al., 2015, MNRAS, 446, 521
Scodeggio M. et al., 2018, A&A, 609, A84
Sembach K. R. et al., 2003, ApJS, 146, 165
Shapley A. E., Steidel C. C., Pettini M., Adelberger K. L., 2003, ApJ, 588, 65
Shimmins A. J., Day G. A., Ekers R. D., Cole D. J., 1966, Aust. J. Phys., 19, 837
Shopbell P. L., Bland-Hawthorn J., 1998, ApJ, 493, 129
Shull J. M., 2014, ApJ, 784, 142
Shull J. M., Smith B. D., Danforth C. W., 2012, ApJ, 759, 23
Simcoe R. A., Sargent W. L. W., Rauch M., Becker G., 2006, ApJ, 637, 648
Sobral D., Smail I., Best P. N., Geach J. E., Matsuda Y., Stott J. P., Cirasuolo M., Kurk J., 2013, MNRAS, 428, 1128
Soto K. T., Lilly S. J., Bacon R., Richard J., Conseil S., 2016, MNRAS, 458, 3210
Steidel C. C., Dickinson M., Persson S. E., 1994, ApJ, 437, L75
Steidel C. C., Kollmeier J. A., Shapley A. E., Churchill C. W., Dickinson M., Pettini M., 2002, ApJ, 570, 526
Stern J., Faucher-Giguère C.-A., Hennawi J. F., Hafen Z., Johnson S. D., Fielding D., 2018, ApJ, 865, 91
Stern J., Hennawi J. F., Prochaska J. X., Werk J. K., 2016, ApJ, 830, 87
Stocke J. T., Keeney B. A., Danforth C. W., Oppenheimer B. D., Pratt C. T., Berlind A. A., 2017, ApJ, 838, 37
Stocke J. T. et al., 2014, ApJ, 791, 128
Struble M. F., Rood H. J., 1999, ApJS, 125, 35
Swinbank A. M. et al., 2010, Nature, 464, 733
Tacconi L. J. et al., 2010, Nature, 463, 781
Tejos N., Morris S. L., Crighton N. H. M., Theuns T., Altay G., Finn C. W., 2012, MNRAS, 425, 245
Tejos N. et al., 2014, MNRAS, 437, 2017
Tejos N. et al., 2016, MNRAS, 455, 2662
Tripp T. M., Aracil B., Bowen D. V., Jenkins E. B., 2006, ApJ, 643, L77
Tripp T. M., Giroux M. L., Stocke J. T., Tumlinson J., Oegerle W. R., 2001, ApJ, 563, 724
Tripp T. M., Savage B. D., Jenkins E. B., 2000, ApJ, 534, L1
Tripp T. M., Sembach K. R., Bowen D. V., Savage B. D., Jenkins E. B., Lehner N., Richter P., 2008, ApJS, 177, 39
Tripp T. M. et al., 2011, Science, 334, 952
Tumlinson J. et al., 2011, Science, 334, 948
Tumlinson J. et al., 2013, ApJ, 777, 59
Tummuangpak P., Bielby R. M., Shanks T., Theuns T., Crighton N. H. M., Francke H., Infante L., 2014, MNRAS, 442, 2094
Turner M. L., Schaye J., Crain R. A., Rudie G., Steidel C. C., Strom A., Theuns T., 2017, MNRAS, 471, 690
Turner M. L., Schaye J., Steidel C. C., Rudie G. C., Strom A. L., 2015, MNRAS, 450, 2067
van de Voort F., 2017, in Fox A. J., Davé R., eds., Astrophysics and Space Science Library, Vol. 430, Gas Accretion on to Galaxies. Springer International Publishing AG, New York, p. 301
van de Voort F., Schaye J., Booth C. M., Dalla Vecchia C., 2011, MNRAS, 415, 2782
Wake D. A. et al., 2011, ApJ, 728, 46
Wakker B. P., Savage B. D., 2009, ApJS, 182, 378
Wakker B. P. et al., 2003, ApJS, 146, 1
Weilbacher P. M., Streicher O., Urrutia T., Pécontal-Rousset A., Jarno A., Bacon R., 2014, in Manset N., Forshay P., eds, ASP Conf. Ser. Vol. 485, Astronomical Data Analysis Software and Systems XXIII. Astron. Soc. Pac., San Francisco, p. 451
Werk J. K., Prochaska J. X., Thom C., Tumlinson J., Tripp T. M., O'Meara J. M., Peeples M. S., 2013, ApJS, 204, 17
Werk J. K. et al., 2014, ApJ, 792, 8
Werk J. K. et al., 2016, ApJ, 833, 54
Woodgate B. E. et al., 1998, PASP, 110, 1183
Zahedy F. S., Chen H.-W., Johnson S. D., Pierce R. M., Rauch M., Huang Y.-H., Weiner B. J., Gauthier J.-R., 2019, MNRAS, 484, 2257

SUPPORTING INFORMATION

Supplementary data are available at *MNRAS* online.

Figure S1 Example objects from the *HST* WFC3 grism data. In each case the top-left panel shows the median spectrum (orange) and contamination-masked mean spectrum (dark red). The lower-left panel in each case shows the corresponding spectra taken at each roll angle, whilst the right-hand panel in each case shows a thumbnail taken from the WFC3 *F*140*W* stacked image.

Please note: Oxford University Press is not responsible for the content or functionality of any supporting materials supplied by the authors. Any queries (other than missing material) should be directed to the corresponding author for the article.

This paper has been typeset from a TEX/LATEX file prepared by the author.